Article

Experimental and Numerical Study on the Flexural Behaviors of Unbonded Prestressed I-Shaped Steel Encased in Ultra-High-Performance Concrete Beams

Nianchun Deng [1,2,*] , Yanfeng Deng [1], Jiqiang Duan [1] and Wenhao Xue [1]

[1] College of Civil Engineering and Architecture, Guangxi University, Nanning 530004, China; dengyanfengguofu@163.com (Y.D.); ztmbec218@163.com (J.D.); 13333756367@163.com (W.X.)
[2] Key Laboratory of Disaster Prevention and Structural Safety of Chinese Ministry of Education, Guangxi University, Nanning 530004, China
* Correspondence: dengnch@gxu.edu.cn

Abstract: A novel type of traditional composite member-unbonded prestressed I-shaped steel encased in a UHPC (PSRUHPC) beam is proposed to reduce the brittleness of UHPC beams and improve their bearing capacity. A PSRUHPC beam, an unbonded prestressed UHPC (PRUHPC) beam, and an I-shape steel UHPC (SRUHPC) beam were manufactured, and their flexural static performances were assessed using a flexural comparison test. The test results reveal that the flexural process of the PSRUHPC beam is similar to that of ordinary reinforced concrete beams, and UHPC crushing in the compression zone is a sign of failure. Due to the bridge coupling effect of steel fiber, the crushed concrete still maintains good integrity without bursting, the UHPC in the tension zone remains functional after cracking, and the cracking inflection point of the load–deflection curve was not obvious. The PSRUHPC beam showed a significantly improved bearing capacity and flexural stiffness, its load–deflection curve exhibited significantly more energy consumption, and its bending ductility performance was improved, with better deformation properties. Compared with PRUHPC beams, PSRUHPC beams show a bearing capacity increase of 55.3%, a cracking load increase of 11.9%, and a displacement ductility coefficient increase of 76.2%. Compared with SRUHPC beams, PSRUHPC beams show a 15.4% increase in bearing capacity, a 50.2% increase in cracking load, and a 12.1% increase in displacement ductility coefficient. The application of prestress can significantly improve the stiffness of the beam prior to cracking. The cracking loads of prestressed ordinary concrete beams and steel-reinforced concrete beams account for 20–30% of their ultimate loads, which value was 40–50% for the tested beams. The change trend of strain in the section steel and UHPC is roughly the same at the same height, and the strains of the two deviated after most of the section steel yielded under tension, but they can generally work together. When the tested beams were cracked, multiple cracks appeared, which were fine and dense. The magnetic flux sensor cable force-monitoring system can better monitor the strand stress increment of unbonded prestressed steel UHPC beams, where the prestressed strand did not yield tension under the final state; the load–strand stress increment curve was basically the same as the load–deflection curve, and the stress increment of the unbonded steel strand positively correlated with the midspan deflection. Finite element simulation was used to verify the test results, and we determined the reinforcement ratios for non-prestressed and prestressed reinforcement, as well as the ratio of a steel-containing section, the effective prestress, the height of prestressed reinforcement, the position and strength of I-shaped steel, and whether or not the prestressed reinforcement was bonded. The effects of these parameters on the bearing capacity and displacement ductility coefficient of PSRUHPC beams were studied. The results can provide a reference for subsequent theoretical design calculations.

Keywords: flexural tests; I-shaped steel encased in UHPC; unbonded prestressed; stress increment; magnetic flux sensor; numerical simulation

1. Introduction

Ultra-high-performance concrete (UHPC for short) [1] has become a research hotspot in the field of engineering materials due to its ultra-high strength, high toughness, high durability, high impact resistance, volume stability, and many other excellent properties [2]. UHPC has ultra-high strength and homogeneity, which can be utilized in greatly reducing the cross-sectional size and weight of beam structures, thus easily facilitating applications in long-span heavy loads and having a large use clearance [3,4]. UHPC has excellent permeability resistance and corrosion resistance, and good wear resistance [5], which can provide sufficient security when used for structures in complex and harsh environments, while improving the life of the structure and reducing the economic costs of the whole life cycle. When UHPC is used in actual engineering, the amount of carbon dioxide and harmful gases emitted during the preparation process is greatly reduced compared with ordinary concrete, making it more green, environmentally friendly, and energy-saving [6]. UHPC has no coarse aggregates, and the particles are mostly densely packed and mixed with fibers, which are the basis of its good fracture toughness [7], allowing structures in which it is used to have greater free deformation and plastic deformation, thereby potentially improving the dynamic performance of the structure [8,9] and its anti-knock and impact resistance [10,11].

Experiments are the most intuitive and effective way to study the mechanical properties of new structural components. Bending resistance is one of the basic mechanical properties of beam components, and many scholars are engaged in research on the bending performance of UHPC beams. Baek-II et al. [12] determined the bearing capacity of nine different cross-sectional stress distribution forms of UHPC beams, and compared them with experimental results, thus obtaining a suitable bearing capacity calculation method. Singh et al. [13] used ABAQUS to simulate the bending performance of UHPC beams with different spans, and compared the results with experiments to verify the reliability of finite element simulation. Chen et al. [14] studied the changes in flexural performance of UHPC beams with different reinforcement ratios through experiments, proposed a formula for estimating bearing capacity, and compared it with test values. Liu et al. [15] validated the formula proposed for calculating the flexural bearing capacity of the normal section through four-point bending tests of UHPC beams, and compared its findings with simulated values and experimental results. At the same time, they also compared it with the standard formulae of France and Sweden to demonstrate the feasibility of the theoretical formula. Qiu et al. [16] conducted experiments to study the bending performance of UHPC beams with different reinforcement ratios, fiber types, and fiber aspect ratios, and proposed a formula for calculating the bending bearing capacity.

However, because the elastic modulus of UHPC is not improved as much as its strength, when used in a structure that is high-strength and lightweight, its rigidity needs to be improved through its structural design. Although UHPC has an ultra-high compressive strength and fiber improves its toughness, it still shows greater brittleness when broken. Reinforced UHPC beams can show improved partial bending performance, but the strain hardening characteristics of UHPC and the high adhesive strength of steel bars can lead to the strain concentration of steel bars in the crack zone, thereby weakening the ductility of the structure [17]. Hence, it is necessary to avoid brittle failure through structural innovation design. The unit price of the UHPC material is high, and structural innovation is also required to give full play to the advantages of the material [18,19].

The solution to the brittle failure problem of UHPC can be obtained from assessments of ordinary concrete. Civil construction engineers are also focusing on combinations of building materials to improve the toughness and bearing capacity of concrete beams [20,21]. Beams made of shaped steel encased in concrete are a type of steel–concrete composite structure, referring to composite beams made of rolled or welded steel beams built into ordinary concrete beams. They have been widely used in high-rise, super-high-rise, and large-span heavy-duty structures. For beam members with strict deformation and crack control, prestress is required to improve the working performance during normal use.

The arrangement of reinforcements in the reinforced concrete beam is complicated, and the unbonded prestressed construction is simpler than bonding, but strict anti-corrosion measures are required for the unbonded prestressed reinforcement, and the accurate determination of the stress increment is difficult when the beam is in the state of ultimate bearing capacity [22,23]. Magnetic flux sensors are a novel and effective method used for monitoring the stress state of unbonded prestressed steel bars [24].

Based on the characteristics of UHPC and the application of ordinary concrete in composite structures, many UHPC composite structural beams have been proposed. There have been many studies on the flexural properties of UHPC and ordinary concrete composite beams [25–34], as well as on UHPC and steel beams, through shear connectors [35–40]. However, the studies of section steel UHPC are few, and in-depth experimental and theoretical research is needed. Tu'ma et al. [41,42] studied the flexural properties of 11 beams of hollow steel wrapped in UHPC under two-point loading; the examined variables included the type of hollow core mold material and the size, location, and shape of the hollow steel sections in the middle and tension zones of the cross-section. The test results show that the flexural capacity and stiffness of the UHPC-encased steel hollow beams were 109% and 23.5% higher, respectively, than those of solid beams. Bu et al. [43–46] carried out static flexural performance tests and theoretical studies of the bearing capacity of beams of I-shaped steel encircled with UHPC with different strengths. Huang et al. [47–49] developed a formula for predicting characteristic bond strength between profile steel and UHPC under different influences, as well as the distribution law of bond stress along the anchorage length, and put forward the bond–slip constitutive relationship between profile steel and UHPC. Shao et al. [50] studied the construction, crack resistance, and load-bearing capacity of cast-in-place joints in the negative bending moment zone at the top of the pier of simply supported and then continuous main beams. Ye [51] conducted bending tests on section steel UHPC beams, verified them through numerical simulation, analyzed the influencing factors and parameters, and derived formulas for inferring stiffness and crack width.

Here, a traditional form of new material composite beam is proposed, namely, beams of unbonded prestressed I-shaped encased in UHPC (PSRUHPC), which were developed based on the material properties of UHPC, the structural characteristics of steel encased in concrete beams, and unbonded prestressing technology. Currently, there are no reports on PSRUHPC beams. As the most basic mechanical property of beam members, it is necessary to study flexural resistance in order to provide a reference for the design and calculation of such members in the future.

2. Experimental Program

Experiments are the most intuitive and effective way to study the mechanical properties of new structural components. Bending resistance is one of the basic mechanical properties of beam components, and it is necessary to conduct experimental research on the basic mechanical properties of new components. We herein produce an unbonded prestressed steel UHPC (PSRUHPC) beam, an unbonded prestressed UHPC (PRUHPC) beam, and an I-shape steel UHPC (SRUHPC) beam, and investigate the bending mechanical performance of the PSRUHPC beam through bending tests. The experimental process is shown in Figure 1.

2.1. Specimen Design

A total of 3 simply supported beams with rectangular sections were fabricated in the test, named PSRUHPC, PRUHPC, and SRUHPC. The beam length is 4000 mm, the calculated span is 3700 mm, and the height–span ratio is 1:12.3. The lengths of the shear span and pure bending section are 1300 mm and 1100 mm, respectively, and the specific cross-sectional dimensions are shown in Figure 2. The variables are the steel content ratio and the prestressing reinforcement ratio (see Table 1). To date, there have been many studies on UHPC materials, but the composition materials and mixing ratios of UHPC are not uniform, and the properties also differ. Configuring a UHPC, when it has not

been conducted before, can consume a lot of time and money. In most studies on the mechanical properties of prestressed UHPC beams and ordinary reinforced UHPC beams, laboratory-configured UHPC materials have been used, but this is not conducive to the popularization and application of UHPC. For testing, UHPC dry mix SBT-UDC(II) was purchased and used in a mixing ratio of 2071.4 kg of dry mix, 13 kg of water reducing agent, 184.7 kg of water, and 181 kg of steel fiber per cubic meter volume. Q235 grade I14 was adopted for the I-shaped steel, and $1 \times 7\Phi S15.24$ low-relaxation 1860 grade unbonded steel strand was used for the prestressed reinforcement, with a standard value of tensile strength (hereinafter referred to as f_{ptk}) of 1860 MPa, and the tension and compression longitudinal bars were C14 and C10, respectively. The stirrups were A8, the reinforcement ratio met the requirements of strong shear and weak bending, the distance between the support and the beam end was 50 mm, the shear span was 100 mm, and the pure bending distance was 200 mm.
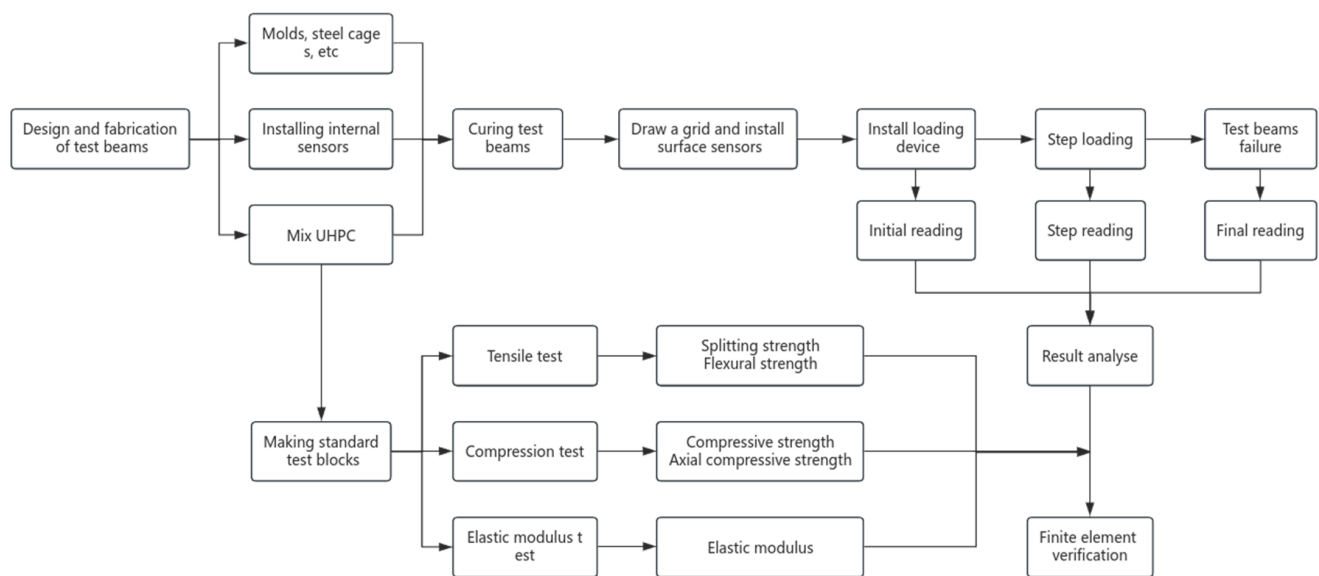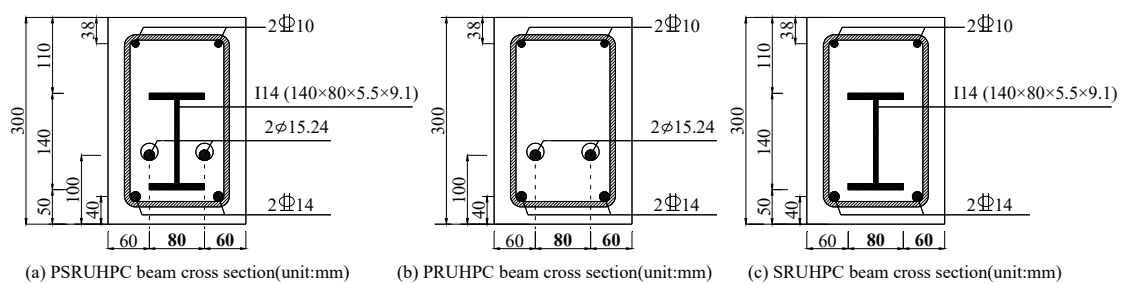

Figure 1. Test process diagram.

(a) PSRUHPC beam cross section(unit:mm) (b) PRUHPC beam cross section(unit:mm) (c) SRUHPC beam cross section(unit:mm)

Figure 2. Cross-section reinforcement diagrams.

Table 1. Composition of the test beams.

Beam Number	I-Shaped Steel (mm)	Prestressed Tendons (Root)	Tension Control Stress (MPa)
PSRUHPC (unbonded prestressed steel UHPC)	$140 \times 80 \times 5.5 \times 9.1$	2	$0.7\,f_{ptk}$
PRUHPC (unbonded prestressed UHPC)	/	2	$0.7\,f_{ptk}$
SRUHPC (unbonded prestressed UHPC)	$140 \times 80 \times 5.5 \times 9.1$	/	/

2.2. Preparation and Maintenance of Specimens

The main steps for preparing the test beam and the test block are as follows: (1) Grind the measuring points of ordinary steel bars and I-shaped steels, paste strain gauges, and protect them with epoxy resin. (2) Bind the steel skeleton, weld short steel bars on the bottom and side of the I-shaped steel to reserve its protective layer, and prepare the wooden formwork according to the designed section size, wherein the formwork will have lateral support and needs to be straight and without deformation. (3) Penetrate the unbonded prestressed steel strands via the holes of the template and embed thin steel plates. There are two magnetic flux sensors on each line, and the height of the prestressed rib is fixed by tying with wire. (4) According to the requirements of the SBT-UDC(II) preparation process, a high-power forced mixer is used for stirring. A single beam is manually poured at a time, and according to the specification [52,53], a cube with a side length of 100 mm, and 100 mm × 100 mm × 300 mm and 100 mm × 100 mm × 400 mm prism test blocks for testing the material's properties are prepared for each beam, under the previous curing conditions. The natural method of maintaining outdoor early watering was adopted, as shown in Figure 3.
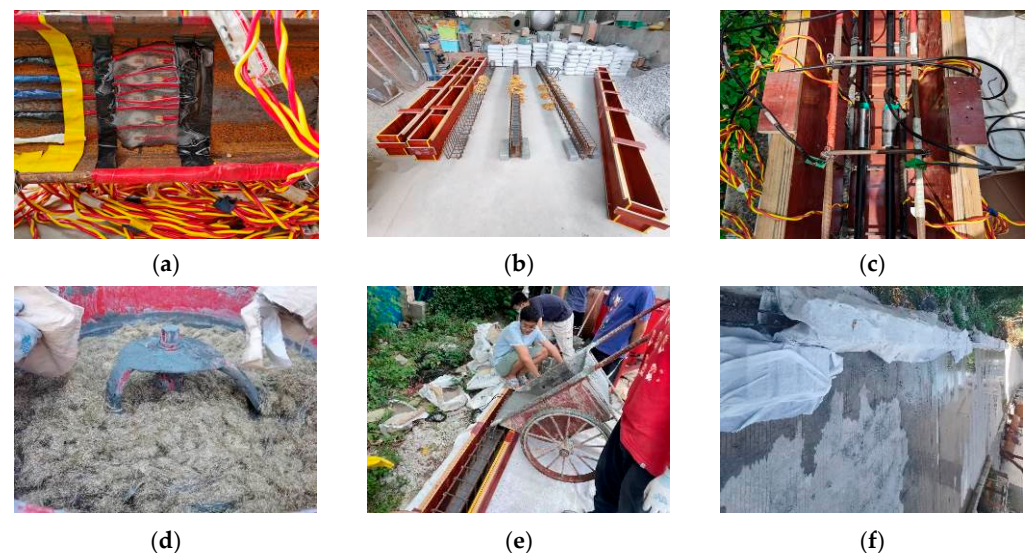

Figure 3. Pouring and curing of specimens: (**a**) pasting strain gauges; (**b**) preparation of wooden formwork; (**c**) magnetic flux sensors on the steel stand; (**d**) stirring and adding of steel fiber; (**e**) pouring UHPC; (**f**) curing of specimens.

(5) When the strength of UHPC reaches 0.75 times the design strength, the prestressed tendons are tensioned, and the magnitude of the prestressed force is controlled by the pressure sensor. After the tensioning control stress is reached, the tensioning end is anchored, as shown in Figure 4. In the prestressing stage, the magnetic flux sensor system [54] is used to obtain the effective prestress of the steel strand, and the dial gauge is used to measure the deflection deformation at the midspan position of the beam. (6) The putty powder slurry is applied to the surface of the beam, and after whitening, 50 mm × 50 mm squares are popped up on both sides of the beam using an ink fountain to observe the development of cracks.

2.3. Loading Scheme and Test Content

The layout of the measuring points and the specific loading device used in the test is shown in Figure 5. Using four-point bending loading, 50% of the cracking load is pre-compressed, and the load is held for 5 min after loading to check whether the support is stable and whether the instrument and loading equipment are normal. The next step is formal loading. Before loading to 90% of the estimated value of the cracking load, the load of each level is kept at 20% of the calculated value of cracking load, and then held for 5 min,

with the collection of data after the load is stable; after reaching 90% of the estimated value of cracking load, with 5% increments, the load is held for 5 min, and then the cracking load is applied and held for 10 min. After the load is stabilized, the data are collected, and the crack distribution is plotted; after the specimen has cracked, 5% of the estimated value of the bearing capacity is taken for each level of load.

(a)   (b)   (c)
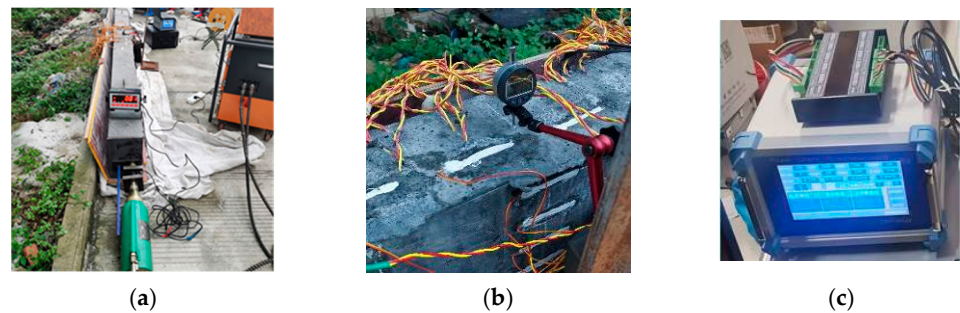
Figure 4. Tension steel strand site: (**a**) oil pump tensioning system; (**b**) midspan arch measurement; (**c**) magnetometer.

(a)

(b)

(c)

(d)
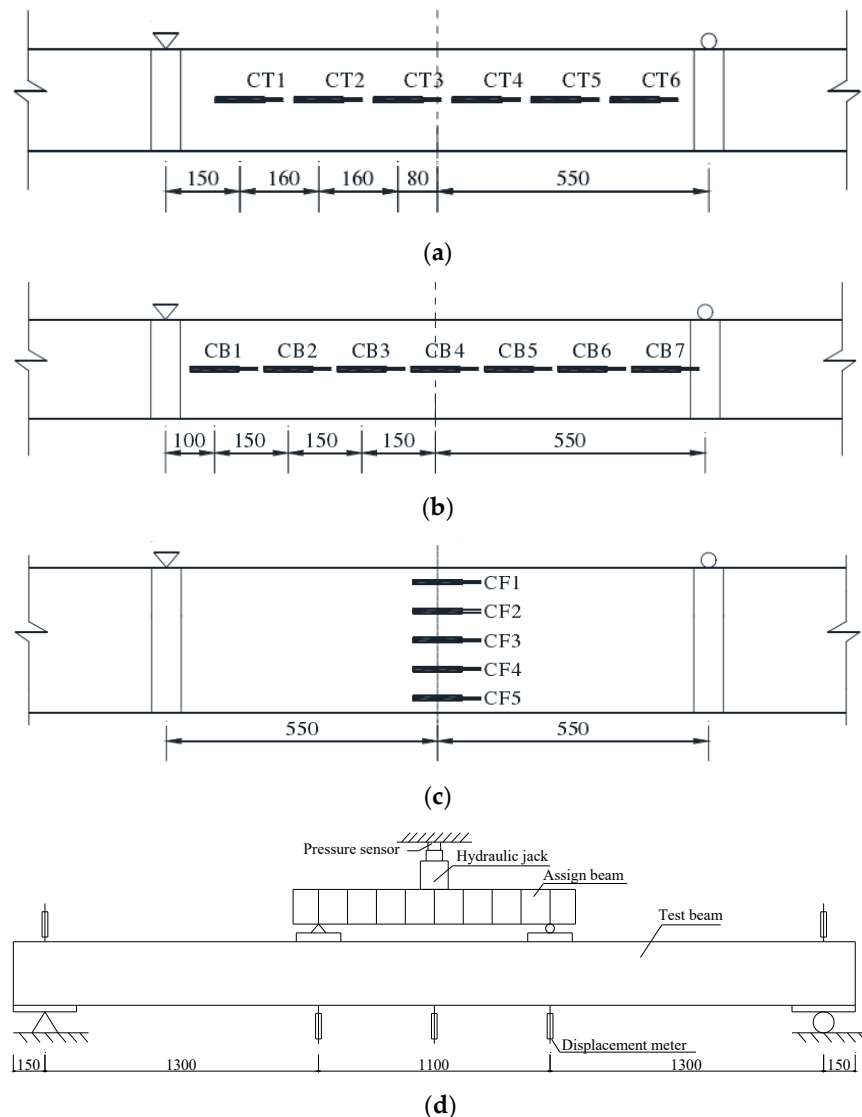
Figure 5. The layout of test. (**a**) Strain gauges in the top compression zone; (**b**) strain gauges in the bottom tension zone; (**c**) strain gauges on the side; (**d**) displacement meter and loading device.

The main equipment used for the measurement is shown in Figure 6. The vertical load is reflected and controlled by the pressure sensor set on the hydraulic oil pump; strain gauge measuring points are arranged to measure the strain value of steel bars and sections; the magnetic flux sensor cable force-monitoring system is used to measure the magnetic flux changes at the midspan and fulcrum of unbonded prestressed steel strand bars during pre-tensioning and loading; the strain value of UHPC is taken at each measuring point of the beam's midspan section; the vertical displacement of the beam at the two supports, two loading points, and midspan is measured, and the position and average spacing of the main cracks under various loads are measured, along with the crack gauge width.

(a)	(b)	(c)	(d)

Figure 6. Main test equipment: (**a**) steel bar strain measuring point; (**b**) UHPC strain gauge points; (**c**) unbonded prestress incremental measurement; (**d**) crack width measurement device.

3. Test Results

3.1. UHPC Material Properties

UHPC test blocks were constructed and subjected to compressive tests, tensile tests, and elastic modulus tests. The obtained compressive strength, axial compressive strength, splitting strength, flexural strength, and elastic modulus were taken for use in finite element simulation. The main equipment of the UHPC material performance test is shown in Figure 7. The maximum compressive strength of the three groups of cube specimens is 140.8 MPa, the minimum compressive strength is 121.2 MPa, and the average value is 132.05 MPa. The average difference between the intermediate value and the most extreme value is 6.6%, which is slightly greater than the theoretical value by 5%, with a small error. The average value is taken as the cube compressive strength of SBT-UDC(II). This is 94.7 MPa for the first group, 86.5 MPa for the second group, and 115.9 MPa for the third group. The difference between the medium value of 94.7 MPa and the minimum value of 86.5 MPa is 8.7%, which is greater than 5%, but not more than 15%. The error is within an acceptable range. The average value, 99 MPa, is used as the axial compressive strength.

The splitting tensile strength fi_{ts} obtained from the actual measurement of the splitting failure load and the splitting area of the three test blocks is 7.8 MPa for the first group, 15.6 MPa for the second group, and 10.6 MPa for the third group, and the middle value of 10.6 MPa is taken as the split crack tensile strength.

The bending tensile strength obtained from the measurement of the bending failure load and cross-sectional area of the three test blocks is 17.2 MPa for the first group, 16.4 MPa for the second group, and 25.1 MPa for the third group. Since the failure cracks of the third group of test blocks are located outside the pure bending section, the data of the test blocks are invalid, and the mean value of the first two groups of 16.8 MPa is taken as the flexural strength.

The three measured elastic modulus values are 52,638.3 MPa for the first group, 53,598.5 MPa for the second group, and 53,851.6 MPa for the third group; the average value of the three is 53,362.8 MPa, which is taken as the initial elastic modulus of SBT-UDC(II).
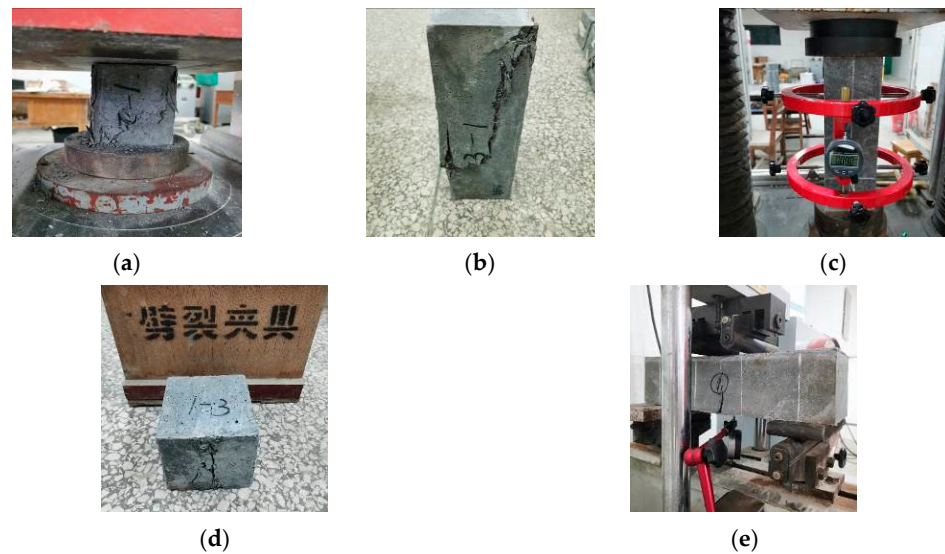
Figure 7. UHPC material performance test: (**a**) cube compression; (**b**) compression of the prismatic axis; (**c**) prismatic modulus of elasticity; (**d**) cube split tensile (the text means 'splitting fixture'); (**e**) prism bending tensile.

3.2. Test Process and Phenomenon

A PSRUHPC beam, a PRUHPC beam and an SRUHPC beam were made and subjected to bending tests to investigate their flexural mechanical properties.

3.2.1. Loading the Destruction Process

Taking the PSRUHPC beam as an example, in the initial stage of loading, the strain of the steel and concrete increased linearly, the deflection increased slowly, and there was no crack that could be observed by the naked eye or instruments. When loaded to 80 kN, 24 vertical micro-cracks appeared in the pure bending section on both sides of the PSRUHPC beam, and some of the micro-cracks did not crack from the bottom edge of the beam. The crack height did not reach the height of the longitudinal tensile steel bars (40 mm). With the increase in the load, the number of cracks in the pure bending section and shear span section continued to increase, and the existing cracks continued to expand and extend upward or downward. When the load reached 98.32 kN, another 17 micro-cracks were added in the two sides. The crack width was too small to measure, and the crack height exceeded the edge height of the steel bottom plate (50 mm). When the load was 118.04 kN, 21 micro-cracks emerged and continued to increase on both sides; the maximum crack width was 0.033 mm, and the maximum crack height was 98 mm. The load at this level was considered to be the cracking load, and the midspan deflection was 6.3 mm; when the load reached 138.19 kN, 15 cracks emerged on both sides. The maximum crack width was 0.041 mm, and the maximum crack height was 137 mm. When loaded to 159.3 kN, five cracks emerged and continued to increase on both sides; the maximum crack width was 0.052 mm, and the maximum crack height was 156 mm. When loaded to 180 kN, the bottom plate of the I-shaped steel yielded under tension, and then 15 cracks emerged on both side. The maximum crack width was 0.073 mm, the maximum crack height was 168 mm, and the midspan deflection was 12.1 mm. When the load reached 206.07 kN, the longitudinal tensile steel bars began to yield, and 9 new cracks appeared on both sides of the beam, while 106 cracks appeared overall. The maximum crack width was 0.092 mm, the maximum crack height was 180 mm, and the midspan deflection was 16.6 mm. When the PSRUHPC beam was flexed and cracked, multiple cracks appeared; the cracks were thin and dense, and they started around the first crack. These micro-cracks did not start from the bottom of the beam, and the initial cracking directions were diverse and not perpendicular to the bottom edge of the beam.

These phenomena indicate that with additional loading, the existing crack width and height and continued to expand. The bending–shear oblique cracks in the bending–shear section extended obliquely from the lower edge of the beam to the loading point. In the later stage of loading, from the yield load of the steel bar to the ultimate load, the crack width and height developed rapidly, and three main cracks were gradually formed at the tension zone, while the hissing sound of fibers pulling out at the cracks could be heard. When the load reached 298.75 kN, the maximum crack width in the tension zone was 0.683 mm, and the maximum crack height was 215 mm. Horizontal cracks appeared in the UHPC in the compression zone; the steel fibers became exposed, and the powder was continuously peeled off but not cracked, making a crackling sound. The UHPC in the pressure zone was crushed, and the pressure sensor reading began to drop. The oil pump could not continue to pressurize, the beam could not hold the load, and the PSRUHPC beam failed; the limit of the midspan deflection in this state was 60.7 mm. Figure 8 shows the PSRUHPC beam before loading, during the ultimate bearing capacity state, and after the test when completely unloaded.

(**a**)	(**b**)
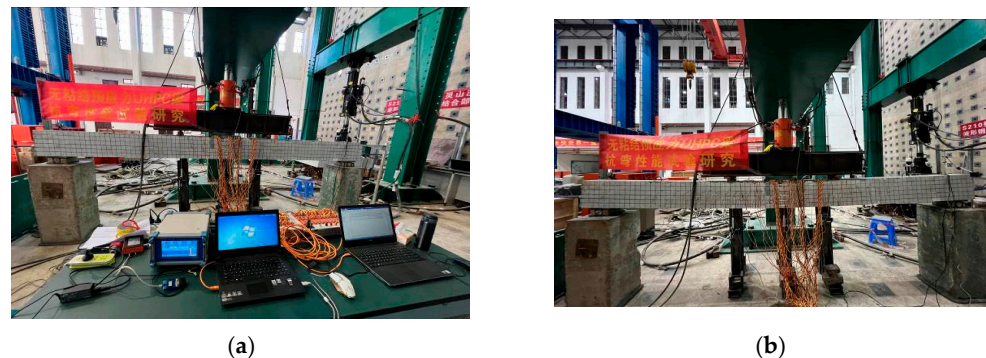
Figure 8. The loading process of the PSRUHPC beam test (the banner means 'Experimental Study on the Bending Performance of Unbonded Prestressed UHPC Beams'): (**a**) PSRUHPC beam before loading; (**b**) completely unloaded after the test.

3.2.2. Damage and Fracture Distribution

Taking the PSRUHPC beam as an example, after reaching the cracking load, the height of the neutral axis increased slightly. With the increase in the load, the cracks continued to develop, and the neutral axis gradually moved upward. When the load reached the longitudinal tensile steel bars' yield point, uniform cracks appeared, and three wide main cracks were formed in the pure bending area; due to the offset of the section steel, the bottom plate yielded first, and the tensile longitudinal bars then yielded. The width and height of the cracks developed rapidly, while the section steel web also gradually yielded under tension, and the neutral axis quickly increased. Finally, the UHPC in the compression zone was crushed. Due to the tie effect of steel fibers, the crushed concrete still maintained good integrity, and there was no fragmentation phenomenon, which manifested as the ductile failure of the reinforced beam. The stress of the prestressed steel strand was evenly distributed along the entire length, and the steel strand did not yield under tension when it failed. Figure 9 shows the crushed concrete in the compression zone of the PSRUHPC beams and the distribution of cracks in the tension zone.

(**a**)   (**b**)

Figure 9. Failure and crack distribution of PSRUHPC beam: (**a**) crushed UHPC; (**b**) three main cracks in the tension zone.

3.3. Analysis of Test Results

3.3.1. Load–Deflection Analysis

Since the force loading method was adopted for the whole process, the test beam could not continue to hold the load when it reached the limit of its bearing capacity, so the descending section of the load–deflection curve was not measured, as shown in Figure 10. It can be seen that the P-f curves of the three test beams have three segments, with a turning point near the characteristic point. The meanings of each curve segment are as follows:
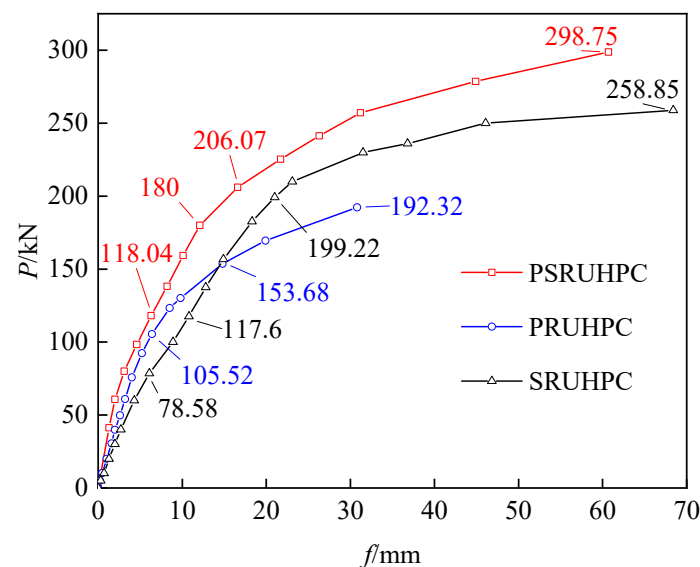
Figure 10. Analysis of load–deflection curves of three test beams.

The first stage is the UHPC cracking, which occurred when the load was applied to the tensile zone of the test beam, and is known as the uncracked elastic stage. When the tensile zone of UHPC was not cracked, the flexural stiffness of the test beam remained basically unchanged and could be taken as a constant. The strain of the built-in I-shaped steel and ordinary tensile steel was small, and the stress of the unbonded prestressed steel increased slowly. The compressive stress and tensile stress of UHPC are basically the same, showing a triangular distribution. The test beam was in the stage of linear elastic deformation, and the load–deflection curve changes more or less linearly here. In the uncracked stage, little difference can be seen in stiffness between the PSRUHPC and PRUHPC beams, and the stiffness contribution of the section steel was small. At the same time, due to the application of prestressing, the stiffness values of the PSRUHPC and PRUHPC beams were obviously greater than those of the SRUHPC beams without prestressing, and because of

the prestressing, the bending stiffness of UHPC beams at the initial stage of loading could be improved;

The second stage shows the UHPC at the bottom of the test beam cracking until the section steel and ordinary steel bar yielded under tension. For PSRUHPC and SRUHPC beams equipped with Q235-graded section steel, the bottom plate of the I-shaped steel yielded before beams with HRB400-grade ordinary steel. After the test beam was cracked, the UHPC in the tension zone continued to function due to the steel fiber bridge connection. Part of the tension originally borne by the UHPC was immediately borne by the tensile longitudinal reinforcement and the tension part of the section steel, and the internal force within the tension longitudinal reinforcement and I-shaped steel was redistributed. The bending stiffness of the section decreased slightly, at which point the load–deflection curve shows it first inflection point, although this is not obvious. The load continued to increase until the PSRUHPC and SRUHPC beams' I-shaped steel bottom plates yielded under tension, at which point the curve deviates slightly, but the bearing capacity of the test beam continued to increase linearly. The load continued to increase until the ordinary steel bar yielded under tension, at which point the load–deflection curves of the three test beams all show a second obvious inflection point, and the load–deflection curves of the test beams begin to slope downwards. According to the measured data for the steel bar and I-shaped steel bar's strain, it can be judged that the lower flange of the section steel yielded first, and so the tensile yield of the ordinary steel bar in the PSRUHPC and SRUHPC beams has been used as a sign of the commencement of the yield state. In the crack-to-yield stage, the flexural stiffness values of the PSRUHPC and PRUHPC beams decreased less notably due to prestressing compared to the SRUHPC beams, and the prestressed beams still showed greater stiffness than the un-prestressed beams. The flexural stiffness values of the PRUHPC beams began to differ greatly at this stage, and the stiffness of the former was significantly greater than that of the latter. This is due to the built-in section steel of the former, and the contribution of the section steel to the flexural stiffness increased;

The third stage shows the test beam reaching its ultimate bearing capacity. After the non-prestressed longitudinal reinforcement of the test beam yielded, the test beam entered the yield stage, that is, the elastic–plastic stage. With the increase in the width and height of the UHPC's cracks in the compression zone, we saw the gradual yielding of the I-shaped steel web, and the increase in the stress of the unbonded prestressed strand; the stiffness of the test beam continued to decrease, and the bearing capacity showed a nonlinear increase. With continued loading, the top plate of the I-shaped steel yielded under tension; that is, the full section yieldsed, and the UHPC at the edge of the compression zone then reached the ultimate compressive strain and was crushed, after which the test beam reached its ultimate bearing capacity state. Since UHPC does not contain coarse aggregate and is mixed with steel fibers to a certain volume ratio, it has ultra-high toughness, and the UHPC within the protective layer did not collapse under the ultimate load. Since this test adopted force loading, once the peak bearing capacity was reached, the hydraulic oil pump could not continue to load, so the residual bearing capacity of the built-in steel beam could not be shown. At the stage of yielding to the ultimate state, due to the presence of the section steel, the yield platforms of the PSRUHPC and SRUHPC beams were significantly longer than those of PRUHPC beams without built-in section steel, and the load growth values after yielding were also significantly greater than those of PRUHPC beams. Due to the effect of applied stress, the stiffness of PSRUHPC was still greater than that of the SRUHPC beam, but the deflection under ultimate load was smaller than that of the SRUHPC beam.

The cracking, yield, and ultimate loads of the three test beams are shown in Table 2. The results show that the ratios of the cracking load to the ultimate load of PSRUHPC and PRUHPC beams are 39.5% and 54.9%, respectively, which are much higher than those of the prestressed steel ordinary concrete beams and prestressed ultra-high-strength concrete beams, at 25–30% [55–58], indicating that they can bear a large load before cracking. The use of configuration steel did not significantly increase the cracking load of the UHPC beam, with an increase of only 11.9%. The PSRUHPC contained built-in steel, with a

bearing capacity 55.3% higher than that of the PRUHPC beam, and the configuration of the steel had a lower grade, meaning the bearing capacity could be improved to a great extent, and the deformation performance of the beam could also be significantly improved. The ratio of the cracking load of the SRUHPC beam to its ultimate load was 30.4%, which is higher than the 15–20% achieved by the ordinary section steel concrete beam and the ultra-high-strength section steel concrete beam. The value for the PSRUHPC beam was 50.2% higher than that for the SRUHPC beam due to the application of prestress. The degree of improvement is obvious, with an increase in ultimate bearing capacity of only 15.4%.

Table 2. Measured test beam characteristic values.

Specimen Number	Cracking P_{cr}/kN	I-Shaped Yield P_{sy}/kN	Longitudinal Tendon Yield P_{ry}/kN	Ultimate Load P_u/kN	Destruction Form
PSRUHPC	118.04	180.00	206.07	298.75	I-shaped steel, ordinary steel yielding, UHPC crushing in the compression zone
PRUHPC	105.52	/	153.68	192.32	Ordinary steel bar yielding, UHPC crushing in the compression zone
SRUHPC	78.58	117.6	199.22	258.85	I-shaped steel, ordinary steel yielding, UHPC crushing in the compression zone

3.3.2. Strain Analysis of Midspan Section

UHPC and section steel. The strain distributions in the vertical direction of the UHPC section and the steel section of the three test beams in the midspan are shown in Figure 11. From the strain distribution of the three specimens, the following can be determined: (1) In the initial stage of loading, the strain of UHPC in the vertical direction showed a robust linear relationship. After the UHPC cracked, the UHPC strain in the beam height direction showed nonlinear characteristics in the tension zone, but linear characteristics overall. After the steel bar and the full I-shaped steel yielded under tension, the nonlinear characteristics of strain in the height direction became more obvious. In general, the average strain of the plane section of the PSRUHPC beam can be basically inferred. (2) The ultimate compressive strain ε_{cu} of UHPC can be taken as showing a slight change of 3800 $\mu\varepsilon$. (3) In the early stages of test beam cracking, the positions on the neutral axis of the section did not change much, and in the later stage of loading, the neutral axis rose more obviously after the rebar had yielded. (4) There was no longitudinal crack on the surface of the beam body at the junction of the top and bottom plates of the section steel and the concrete in the test, indicating that, as regards the relative relationship between the I-shaped steel and the concrete, the slippage was small, and the I-shaped steel and concrete worked together. There was a certain slip phenomenon between the I-shaped steel and UHPC in the later stage of loading, but the strain in the section steel in the same section showed basically the same change trend as UHPC strain. (5) Before the ultimate load point, the strain change law of the I-shaped section steel section in the direction of the beam's height was similar to that of UHPC. Similarly, due to the offset of the I-shaped section steel, the top plate of the section first underwent compression, then gradual decompression, and then tension, and it finally yielded under tension.

Stress increment of unbonded prestressed steel strands. The magnetic flux change of unbonded prestressed steel strands during the loading process can be measured using the magnetic flux sensor cable force measurement system, and then calculated according to the calibration parameters of the laboratory sensors. Stress increments under graded loads have been plotted as a curve of load–stress increments, as shown in Figure 12. The starting point of the stress increment correlates with the effective prestress. When the steel strand was tensioned in the early stage, the pressure ring and the magnetic flux sensor were used to jointly measure the effective prestress after tensioning. Before formal loading,

the pressure ring was removed, and the magnetic flux sensor was used to measure the effective prestress again. It was found that the difference between the two results could be ignored. It can be seen that the difference in stress increments measured by the sensors placed near the midspan and the fulcrum, respectively, is small, indicating that the stress of the unbonded prestressed strand was uniformly distributed along the entire length.
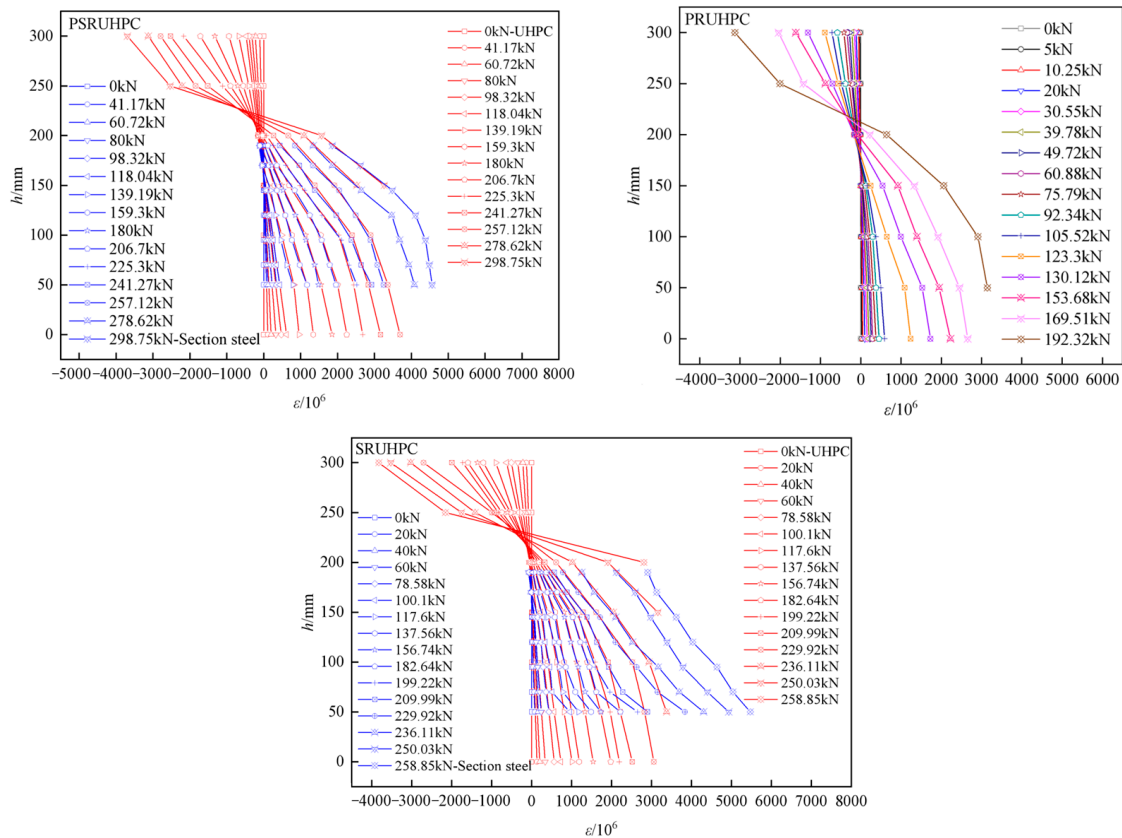

Figure 11. UHPC and I-shaped steel strain of the midspan section of the specimen.
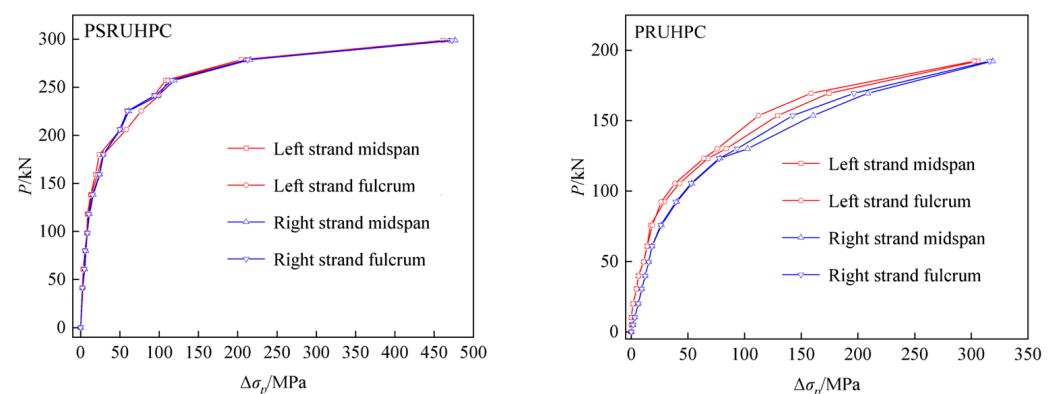
Figure 12. Unbonded prestressed reinforcement load–stress increment.

The shapes of the loaded–unbonded prestressed steel strand stress increment curves for the PSRUHPC and PRUHPC beams are approximately the same as the load–midspan deflection curves, which are also composed of three segments: (1) In the initial stage before and after the cracking of the test beam, the growth in stress of the unbonded prestressed steel strand was very small, the slope of the curve was large, and it basically took the form of a straight line. The external loads were mainly applied to the UHPC in the tension zone,

the profiled steel bottom plates, and the ordinary longitudinal tension steel bars, which provided internal balancing forces. (2) Although the steel fibers in the tension zone of the UHPC played a bridging role, after the cracks had developed to a certain extent, the bonding force between the steel fibers and the matrix at some crack points failed; the stiffness of the specimen thus decreased slightly, and the midspan deflection grew rapidly. The stress growth rate of the bonded prestressed tendons was also accelerated. Ordinary tensile steel and I-shaped section steel worked together with the UHPC, and the stress growth in the two was greater than that of the unbonded prestressed tendons. The load increment at this stage was resisted by the four in combination, and the slope of the curve reflecting this point is reduced. The stress increment of the stress tendons was still low relative to the effective prestress. For PSRUHPC beams, the stress increment of the prestressed steel strands when the UHPC was cracked was only 8.7 MPa. When the steel bottom plate reached the yield strength, the measured stress increment of the unbonded prestressed tendons was 29 MPa, which is only 3% of its effective prestressing force; we also saw the gradual yielding of the section steel web, and the bond force of the steel fiber was lost as the crack developed. The incremental growth rate of the steel strand stress at this point was obvious, and the slope of the curve is significantly reduced. When the longitudinal tensile steel bars yielded, most of the load increment was borne by the steel strands, and the stress of the steel strands thus increased significantly. (3) When the ultimate load was reached, the measured stress increment was 470 MPa; for the PRUHPC beam, the stress increment of the prestressed steel strand when the UHPC cracked was 48.9 MPa. When the reinforcement reached the yield strength, the measured stress increment of the unbonded prestressed reinforcement was 141.1 MPa, which is 17% of its effective prestress. After the longitudinal reinforcement had yielded, the increment in external load was basically borne by the steel strand, which showed stress growth. The slope of the curve is significantly reduced at this point, and the stress increment of the steel strand under the limit state was 310.7 MPa.

3.3.3. Crack Analysis

The three test beams have been divided into two groups for the comparative analysis of crack morphology, as shown in Figure 13, and the following conclusions can be drawn: (1) From the comparison of the test beams PSRUHPC and PRUHPC, it can be seen that the two sides of the unbonded prestressed steel UHPC beam were co-initiated and developed together. There were 106 cracks in total, and 58 cracks developed on both sides of the unbonded prestressed UHPC beams. The former showed more uniform crack widths, smaller average crack spacing, smaller crack heights, and smaller residual maximum crack widths after unloading. (2) The comparison of crack distributions between the PSRUHPC and SRUHPC beams has shown that a total of 98 cracks formed on both sides of the SRUHPC beam. The crack widths of PSRUHPC were significantly smaller than those of SRUHPC, and the crack heights were also lower. The maximum residual crack widths after unloading were also smaller, and the cracks were closer. The performance was better. (3) When the three test beams cracked, multiple cracks appeared. The cracks were fine and dense, and small micro-cracks formed around the first cracks. These micro-cracks did not start from the bottom of the beam. The initial cracking directions were diverse and not perpendicular to the bottom edge of the beam, which may have been due to the bridging effect of the steel fibers, and the fact that the distributions and orientations of the steel fibers in the matrix during pouring were diverse.
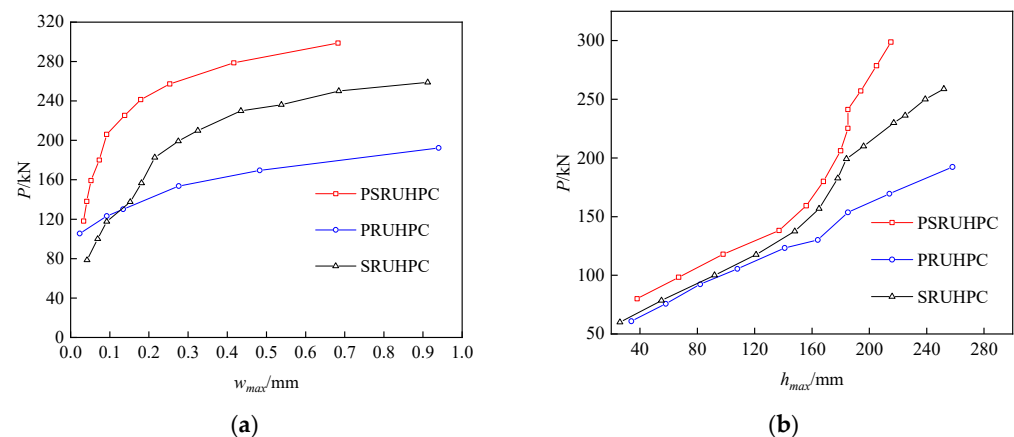
The load–maximum crack width and load–maximum crack height curves of the three test beams are shown in Figure 14. It can be seen that the maximum crack widths of the test beam developed slowly before the yield point, and the crack widths developed significantly after the specimen had yielded. Due to the prestressing process applied to the PSRUHPC and PRUHPC beams, at the initial stage of cracking, the maximum crack widths were smaller than those of the SRUHPC beams without prestressing. Before decompression, prestressing effectively inhibited the development of cracks. PSRUHPC and SRUHPC were

encased in I-shaped section steel, and their maximum crack widths were smaller than those of the PRUHPC beam without I-shaped steel; the crack spacing was smaller and more uniform, and it was seen that the built-in section steel caused the cracks to spread and develop, while slowly consuming and releasing energy. At the beginning of loading, the crack heights of the three test beams developed rapidly. When the cracks had extended to the height of the I-shaped steel web, the crack heights of PSRUHPC and SRUHPC developed slowly due to the blocking effect of the I-shaped steel web. The development of the crack height was accelerated again, and the crack height of the PRUHPC beam developed the fastest overall.
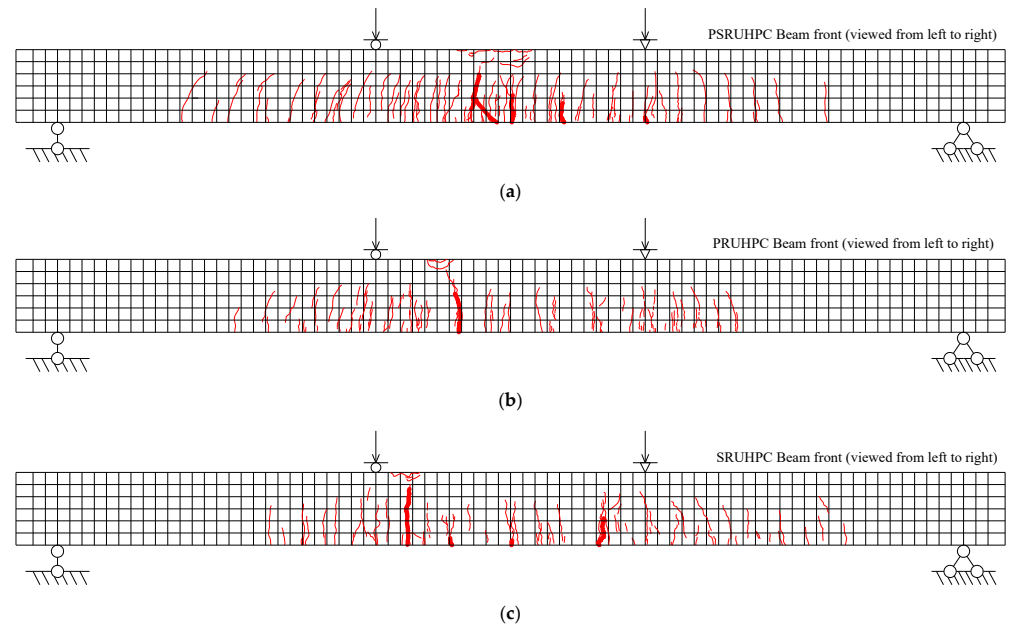
Figure 13. Comparison of test beam cracks for (**a**) PSRUHPC; (**b**) PRUHPC; (**c**) SRUHPC.

Figure 14. Comparison of (**a**) load–maximum crack width and (**b**) load–maximum crack height.

3.3.4. Analysis of Flexural Ductility

As shown in Table 3, the displacement ductility coefficient can be used to describe the ductility, namely, the ratio of the midspan deflection Δu under the ultimate load to the midspan deflection Δy, corresponding to the yield load. In terms of the yield of the longitudinal tensile steel bars, the displacement ductility coefficient of PSRUHPC is better than those of SRUHPC and PRUHPC, with values of 3.7, 3.3, and 2.1, respectively.

Table 3. Ductility index.

Specimen Number	Section Steel Yield Displacement Δ_{sy}/mm	Longitudinal Bar Yield Displacement Δ_{ry}/mm	Limit Displacement Δ_u/mm	Δ_u/Δ_{sy}	Δ_u/Δ_{ry}
PSRUHPC	12.1	16.6	60.7	5.0	3.7
PRUHPC	/	14.8	30.8	/	2.1
SRUHPC	10.8	21.0	68.4	6.3	3.3

4. Nonlinear Finite Element Simulation Analysis

4.1. Material Properties

Fibers were added to the UHPC to endow it with ultra-high strength and high toughness. These beams gave curves with a relatively gentle descending section, which was especially the case for the uniaxial tensile constitutive relationship curve. If the tensile deformation capacity is poor and does not match the ultra-high compressive strength, then during the simulation, serious cracking of the UHPC in the tension zone will occur, the deformation will be too large, and before the concrete in the compression zone has reached its peak stress, the section steel will partially buckle, and the calculation will thus not converge. Therefore, the uniaxial compression constitutive relation proposed by Singh [13] has been selected, wherein the uniaxial tension relation curve offers an approximate strengthening model when combined with the constitutive relation curves mentioned by Su [59], because of their good calculation convergence. Through the measured values of the material characteristics, shown in Table 4, and the conversion formula of the basic mechanical properties of UHPC cited in the literature [60], the corresponding peak strain and ultimate strain can be obtained.

**Table 4.** Material performance parameters (unit: MPa).

	Section Steel	Steel Bars	Stirrups	Strand	SBT-UDC(II)	
Yield strength	235	410	300	1581	Compressive strength	132.05
Ultimate tensile strength	392	480	350	1860	Axial compressive strength	99
Elastic modulus	2.06×10^5	2.0×10^5	2.06×10^5	1.95×10^5	Splitting strength	10.6
/	/	/	/	/	Flexural strength	16.8
					Elastic modulus	5.3×10^4

For all steels, the bilinear strengthening model has been adopted, while the CDP model has been adopted for UHPC. According to the UHPC uniaxial stress–strain relationship curve shown above, combined with the concrete plastic damage model in ABAQUS, the damage factor can be calculated using the energy loss method described in the literature [61], with the other plastic damage parameters being the same as those in the literature [32]. The nominal stress–strain of all materials is in this way converted into real stress–strain, and the elastic–plastic properties of all materials are entered into the material property model in ABAQUS.

4.2. Establishment of Finite Element Model

Taking the PSRUHPC beam as an example, as shown in Figure 15, a rigid spacer was set at the loading point to prevent convergence problems due to stress concentration. Constraints were embedded between the ordinary steel bars, section steels, and UHPC, and bond–slip between the components was thus not considered. Regarding the constraints between the unbonded steel strands and UHPC, we referred to Lou [62], who used a Spring2 element with high stiffness to simulate the behavior in the normal direction and in the transverse tangential direction; here, the longitudinal tangential direction was free to slide, and an MPC-Tie constraint was set at the end node of the steel strand and the UHPC. The elastic modulus of the rigid spacer was set to 10 times the elastic modulus of the steel. The rigid spacer was bound to the UHPC, and two reference points were established above

the spacer for the application of displacement loads. The C3D8R linear reduced-integration element was used for the UHPC, section steel, and rigid spacer, and the T3D2 element was used to simulate the common steel bars and steel strands. The grid sizes of the section steel and UHPC were both 50 mm.
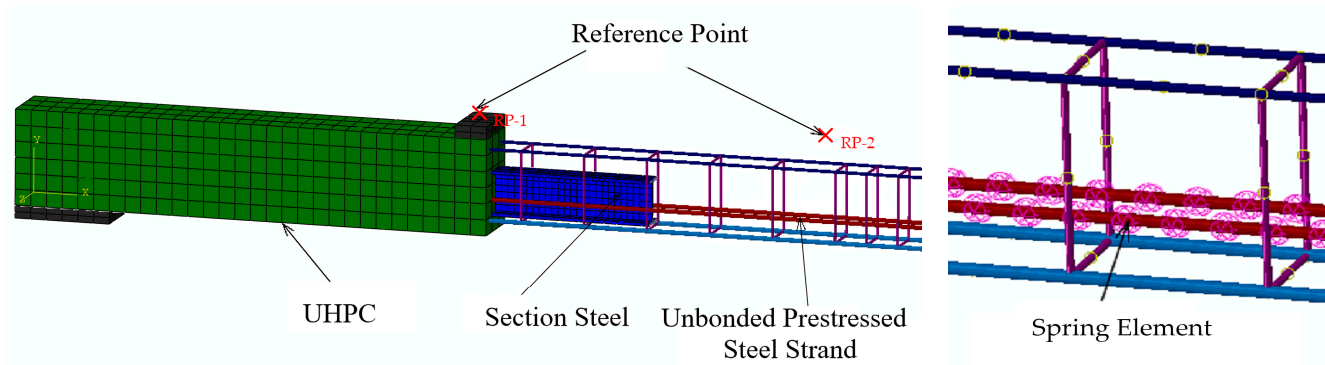

Figure 15. PSRUHPC beam finite element model.

4.3. Verification of Test Results

Comparison of load–deflection curves at midspan. We compared the load–deflection curves obtained by finite element simulation with the test results, as shown in Figure 16. The comparison of the simulated and experimentally derived eigenvalues is shown in Table 5. In the table, P_{cr}, P_{sy}, P_{ry}, and P_u represent the cracking load, the yield load of the profiled steel floor, the yield load of the longitudinal reinforcement, and the ultimate load, respectively. The displacement loading was used in the simulation, and the curve of the descending section was thus obtained. The overall trend of the load–deflection curve that was produced is basically the same as that seen in the test. The PSRUHPC and PRUHPC beams were prestressed in the first step of the analysis. With the application of prestressing, the back-arch values of the midspan were 0.859 mm and 1.023 mm, respectively, as shown in Figure 17, while the measured values of tension were 0.805 mm and 0.962 mm, respectively, and the error was within 5%. In the initial stage of loading, before the UHPC cracked, the simulation curve and the test curve were seen to basically coincide. After cracking, because our simulation ignored the slippage before the reinforcement, section steel, and UHPC, the constraint conditions were more ideal, and the material constitutive relationship produced was different from the actual one, leading to a large analog value. Moreover, due to the fact that the PSRUHPC beam contained both section steel and unbonded prestressed reinforcement, the errors generated by the two were superimposed, resulting in a greater error in the analog values of the PSRUHPC beam. The mean relative errors of the simulated and experimentally derived eigenvalues were 5%, 9%, 10%, and 8%, respectively; these errors are small, which verifies the validity of the finite element model.

Table 5. Comparison of eigenvalues.

Specimen Number	Test Value/kN		Analog Value/kN	Analog Value/Test Value
PSRUHPC	P_{cr}	118.04	112.34	0.95
	P_{sy}	180	213.05	1.18
	P_{ry}	206.07	242.30	1.18
	P_u	298.75	323.13	1.08
PRUHPC	P_{cr}	105.52	104.37	0.99
	P_{ry}	153.68	169.02	1.10
	P_u	192.32	216.86	1.13
SRUHPC	P_{cr}	78.58	71.85	0.91
	P_{sy}	117.6	117.72	1.00
	P_{ry}	199.22	195.46	0.98
	P_u	258.85	266.09	1.03

(a)

(b)

(c)
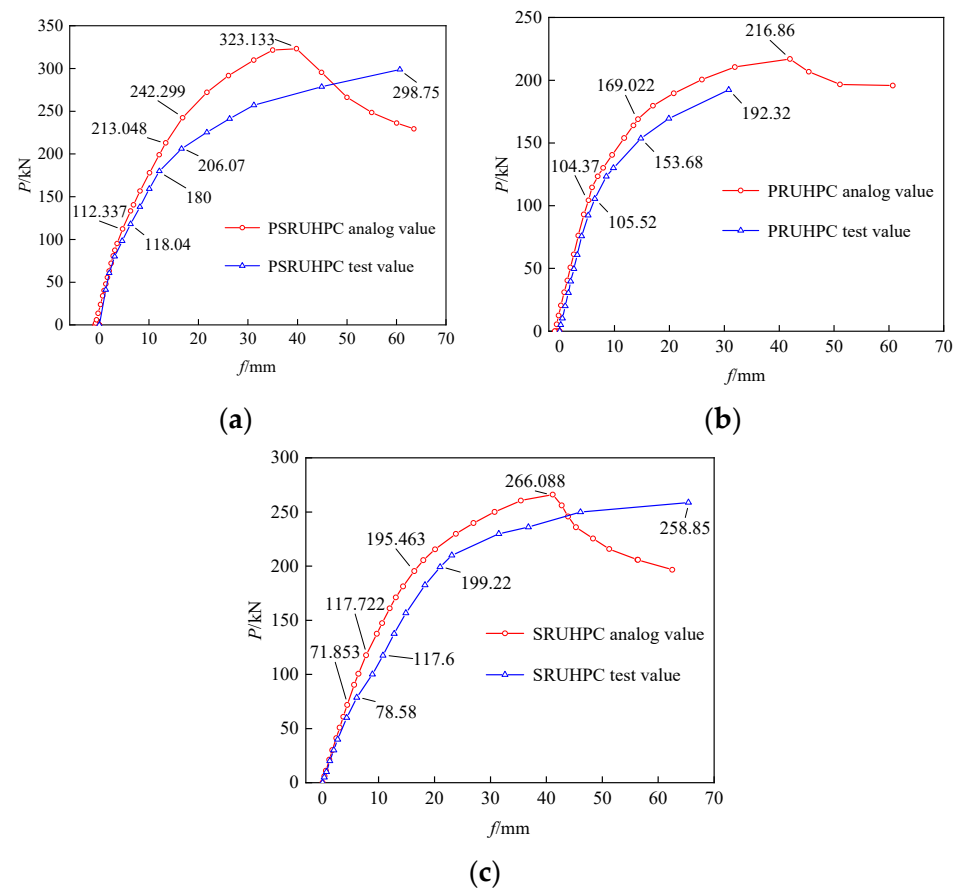
Figure 16. Comparison of simulation and test load–deflection curves: (**a**) PSRUHPC; (**b**) PRUHPC; (**c**) SRUHPC.

Comparison of stress increments. As shown in Figure 18, comparing the simulated stress increments of steel strands with the results of the tests, the simulated load–stress increment curve is roughly the same as the measured curve, and has a similar shape to the load–deflection curve. It can also be seen that the stress increment of the unbonded prestressed steel strand is coupled with the midspan deflection point, via an approximately linear positive correlation. The ultimate bearing capacities of the PSRUHPC and PRUHPC beams were simulated, and the stress cloud diagram of the steel strands is shown in Figure 19. It can also be observed that stress in the unbonded steel strand was uniformly distributed along its entire length.
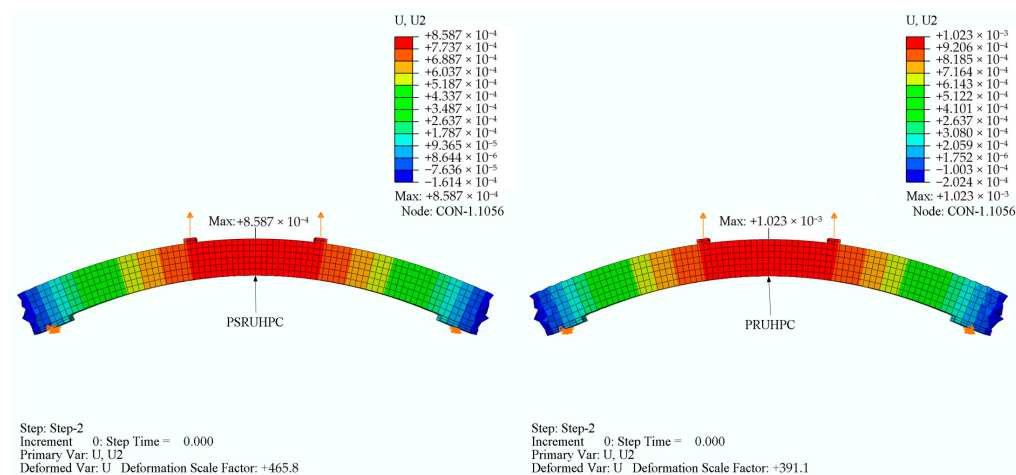
Figure 17. Reverse arch value after tensioning.
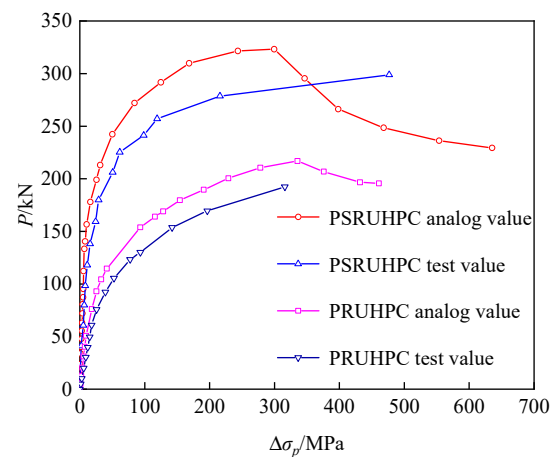
Figure 18. Load–strand stress increment comparison.
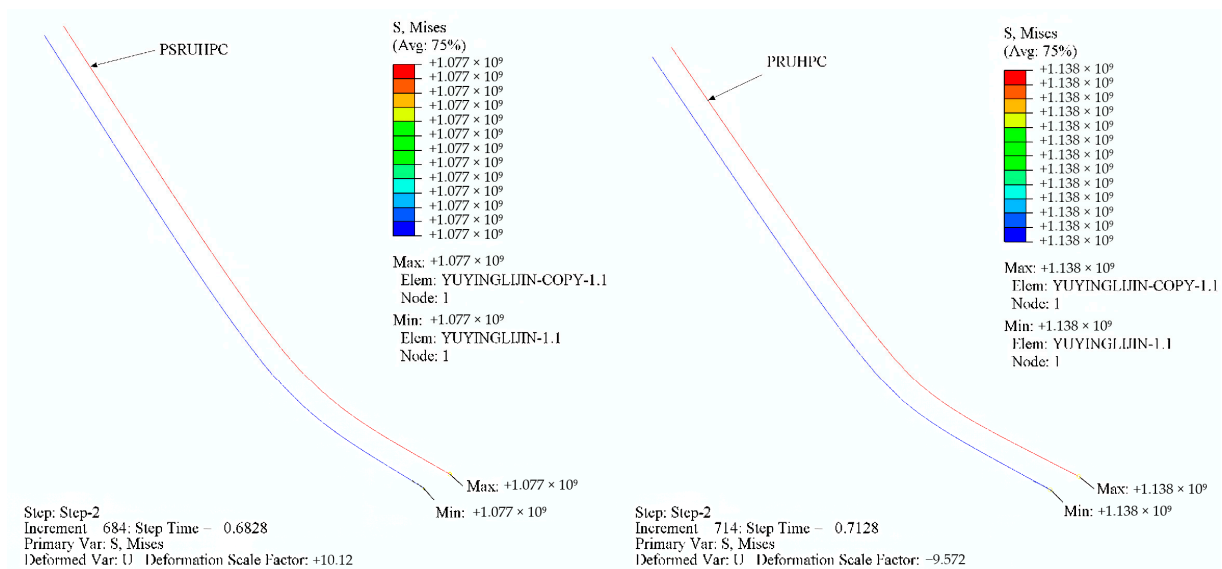
Figure 19. Strand stress at ultimate bearing capacity.

Comparison of failure modes. Taking PSRUHPC as an example, the concrete in the compression zone was crushed, most of the steel bottom plate and web yielded under tension, and the longitudinal bars yielded under tension as well, as shown in Figure 20.

Cracks were compared when the tensile equivalent plastic strain (PEEQ in the ABAQUS 2016 software) was at a certain point εtpl > 0, with the maximum principal plastic strain PE. When the maximum took a positive value, initial cracking occurred, with the normal vector of the crack surface parallel to the direction of maximum plastic strain, as shown in Figure 21.

### 4.4. Analysis of Other Influencing Factors

With the assumption that the finite element model is reliable and correct, the determination of the reinforcement ratio of ordinary steel bars, the reinforcement ratio of prestressed bars, the steel content of section steel, the effective prestress, the heights of prestressed bars, the positions of section steel, the labels of section steel, and the strands of prestressed steel was carried out. The influence of the line being bonded on the flexural bearing capacity and flexural ductility of prestressed steel UHPC beams was studied. The design parameters are shown in Table 6. The parameters of PSRUHPC-01 shown in the table were consistent with the test beam parameters. I14-1, I14-2, I14-3 and I14-4, respectively,

indicate that the section steel web and bottom plate were thickened by 1 to 4 mm, and Q345 and Q420 steel was used.

(**a**)

(**b**)
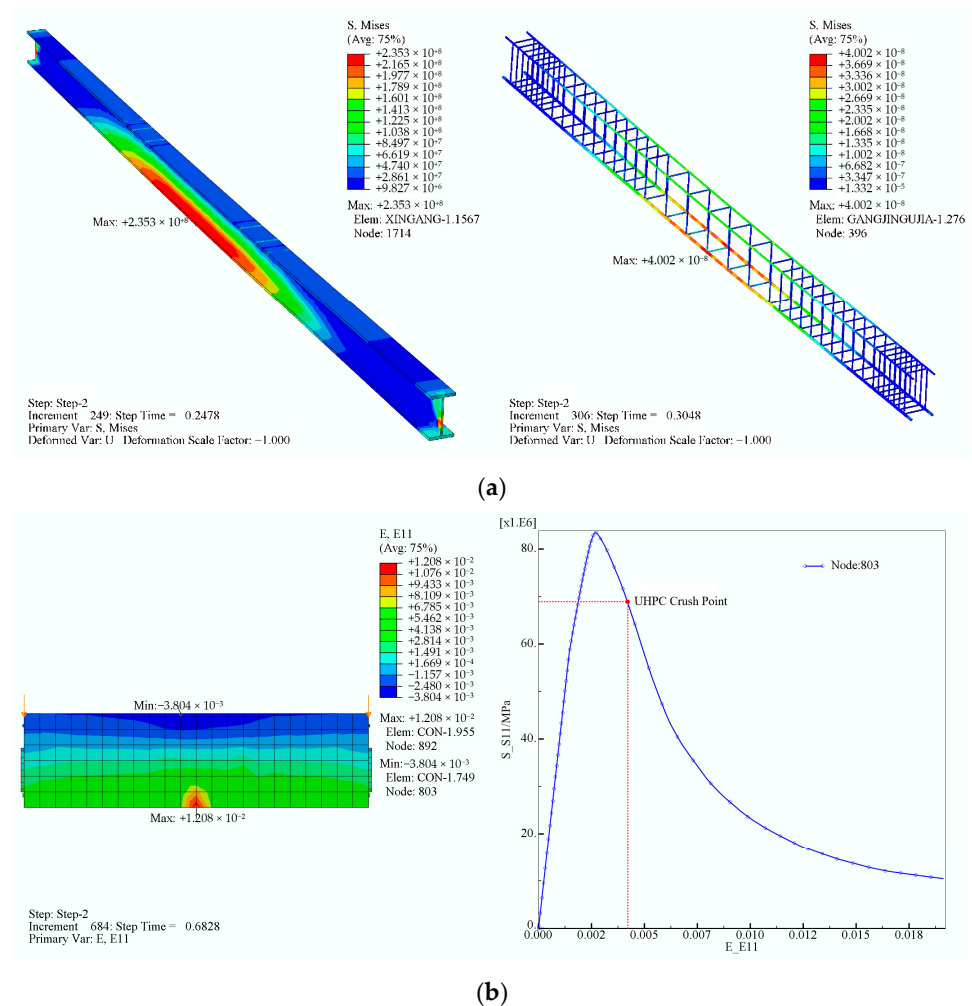
Figure 20. PSRUHPC simulation damage flag. (**a**) Section steel and longitudinal bar yield; (**b**) crushing of UHPC.
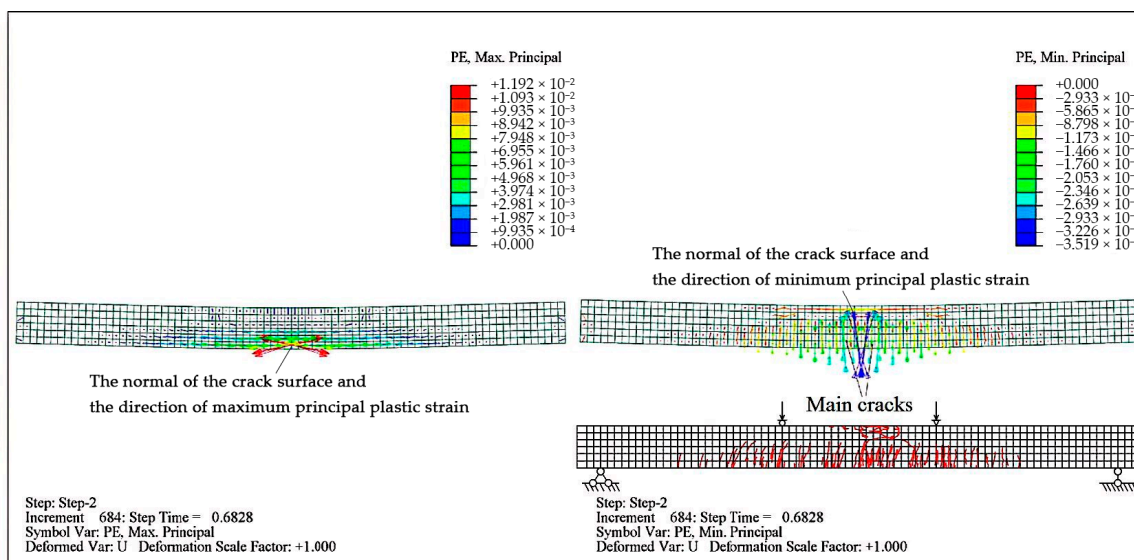
Figure 21. PSRUHPC simulated crack.

Table 6. Design parameters of simulated beams.

Specimen Number	Profile Configuration			Prestressed Tendon Configuration			Tension Longitudinal Bars	Compressed Longitudinal Bars
	a'_s/mm	a_s/mm	Model	A_p/mm^2	h_p/mm	σ_{con}/MPa		
PSRUHPC-01	110	50	I14	278	100	$0.7 f_{ptk}$	2C14	2C10
PSRUHPC-02	110	50	I14	278	100	$0.6 f_{ptk}$	2C14	2C10
PSRUHPC-03	110	50	I14	278	100	$0.8 f_{ptk}$	2C14	2C10
PSRUHPC-04	110	50	I14	278	100	$0.7 f_{ptk}$	2C18	2C10
PSRUHPC-05	110	50	I14	278	100	$0.7 f_{ptk}$	3C18	2C10
PSRUHPC-06	110	50	I14	278	100	$0.7 f_{ptk}$	3C18	3C14
PSRUHPC-07	80	80	I14	278	100	$0.7 f_{ptk}$	2C14	2C10
PSRUHPC-08	80	80	I14	278	100	$0.6 f_{ptk}$	2C14	2C10
PSRUHPC-09	80	80	I14	278	100	$0.8 f_{ptk}$	2C14	2C10
PSRUHPC-10	80	80	I14	278	100	$0.7 f_{ptk}$	2C18	2C10
PSRUHPC-11	80	80	I14	278	100	$0.7 f_{ptk}$	3C18	2C10
PSRUHPC-12	80	80	I14	278	100	$0.7 f_{ptk}$	3C18	3C14
PSRUHPC-13	80	80	I16	278	100	$0.7 f_{ptk}$	2C14	2C10
PSRUHPC-14	80	80	I14	278	50	$0.7 f_{ptk}$	3C18	2C10
PSRUHPC-15	80	80	I14	278	70	$0.7 f_{ptk}$	3C18	2C10
PSRUHPC-16	80	80	I14-1	278	100	$0.7 f_{ptk}$	2C14	2C10
PSRUHPC-17	80	80	I14-2	278	100	$0.7 f_{ptk}$	2C14	2C10
PSRUHPC-18	80	80	I14	197	100	$0.7 f_{ptk}$	3C18	2C10
PSRUHPC-19	80	80	I14	197	50	$0.7 f_{ptk}$	3C18	2C10
PSRUHPC-20	80	80	I14	197	50	$0.6 f_{ptk}$	3C18	2C10
PSRUHPC-21	80	80	I14	197	50	$0.7 f_{ptk}$	2C14	2C10
PSRUHPC-22	80	80	I14	197	50	$0.8 f_{ptk}$	2C14	2C10
PSRUHPC-23	80	80	I14	278	100	$0.7 f_{ptk}$	/	/
PSRUHPC-24	80	80	I14	278	50	$0.7 f_{ptk}$	/	/
PSRUHPC-25	110	50	I14-3	278	100	$0.7 f_{ptk}$	2C14	2C10
PSRUHPC-26	110	50	I14-4	278	100	$0.7 f_{ptk}$	2C14	2C10
PSRUHPC-27	80	80	I14-3	278	100	$0.7 f_{ptk}$	2C14	2C10
PSRUHPC-28	80	80	I14-4	278	100	$0.7 f_{ptk}$	2C14	2C10
PSRUHPC-29	110	50	I14	278	100	$0.7 f_{ptk}$	/	/
PSRUHPC-30	110	50	I14	Same as 1, no bonding			2C14	2C10

4.4.1. Impact on Flexural Capacity

(1)   Reinforcement ratio of ordinary reinforcement

PSRUHPC-01 and 04 have been taken as a group, with the I-shaped beam inclined towards the tensile area. PSRUHPC-07, 10, and 11 comprise another group, with the I-shaped steel in the middle, and the reinforcement ratio of longitudinal tensile reinforcement in each was 0.59%, 0.99%, and 1.48%, respectively. As shown in Figure 22, compared with PSRUHPC-01, the cracking loads of 04 and 05 were increased by 8.4% and 13.3%, the yield loads of the I-shaped beam were increased by 7.3% and 15.9%, the yield loads of tensile steel were increased by 10.4% and 20.7%, and the ultimate loads were increased by 5.1% and 11.9%. Compared with PSRUHPC-07, the cracking loads of 10 and 11 were increased by 3.6% and 8.7%, the yield loads of I-shaped steel were increased by 10.0% and 19.4%, the yield loads of the tensile steel bar were increased by 11.9% and 25.1%, and the ultimate loads were increased by 6.2% and 14.2%. Compared with 21, PSRUHPC-19 manifested a 0.89% increase in the reinforcement ratio of the longitudinal tension bars, an 8.6% increase in their cracking load, a 19.5% increase in I-shaped steel's yield load, a 25.6% increase in tensile steel's yield load, and a 13.5% increase in the ultimate load.

PSRUHPC-29 was not equipped with ordinary steel bars, similarly to 01; the section steel therein was arranged in the tension area, as a result of which the cracking load was reduced by 0.1%, the yield load of the section steel was reduced by 13.6%, and the ultimate load was reduced by 12.5%. PSRUHPC-24 and 23 were not equipped with ordinary steel bars, similarly to 14 and 07; the section steel therein was in the middle, as a result of which the cracking load was reduced by 11.1% and 5.8%, the yield load of the section steel was reduced by 29.2% and 18.1%, and the ultimate load was reduced by 23.3% and 15.1%.

For PSRUHPC-06 and 12, the reinforcement ratios of the compression steel bars increased similarly to 05 and 11, respectively. Compared with 05, the cracking load of

PSRUHPC-06 was increased by 2.6%, the yield load of the section steel was increased 1.3%, the yield load of the tensile steel bar was increased by 1.6%, and the ultimate load was increased by 4.5%. Compared with 06, the cracking load of PSRUHPC-12 was increased by 1.1%, the yield load of the tensile reinforcement was increased by 1.5%, and the ultimate load was increased by 3.9%.

The reinforcement ratio of the longitudinal tensile ordinary steel bar had little effect on the cracking of the concrete in the tensile area. When the reinforcement ratio of the non-prestressed tensile steel bar was increased, the yield load and peak load both showed a linear increase. The reinforcement ratio of compression steel bar had little effect on the cracking load, yield load, or peak load of the specimen, but it improved the bearing capacity of the member after reaching the ultimate bearing capacity, and improved the stability of the residual bearing capacity to a certain extent.

(2)   Reinforcement ratio of prestressed tendons

As shown in Figure 23, the reinforcement ratios of PSRUHPC-18 and 19 in relation to 11 and 14 were reduced from 0.53% to 0.38%, respectively; the simulated beam cracking loads were reduced by 9.6% and 12.3%, the section steel yield loads were reduced by 5.9% and 7.9%, the yield loads of the longitudinal tensile steel bars were reduced by 5.1% and 7.1%, and the ultimate loads were reduced by 3.5% and 5.3%, respectively. Increasing the reinforcement ratio of prestressed tendons can delay beam cracking. In addition to the strength partly imparted in advance, the prestressed tendons showed a large capacity to bear tensile stress, giving the beam a higher bearing capacity, but this improvement of bearing capacity was limited because the beam failure endpoint is the crushing of the UHPC. It can also be seen that the closer the prestressed tendons were to the edge of the beam tension zone, the more obvious this amplification effect was.

(3)   Steel content of section steel

As shown in Figure 24, in relation to 07, PSRUHPC-13, 16, and 17 adopted I14 steel to I16 steel, thickening the web of the I14 steel and thickening the bottom plate of the I14 steel, separately, so as to increase the steel distribution ratio, and the steel contents increases 21.5%, 22.9%, and 15.1%, respectively. Compared with 07, the cracking loads of 13, 16, and 17 increased by 3.8%, decreased by 0.1%, and increased by 1.6%, respectively. The yield loads of the section steel increased by 4.5%, 3.4%, and 9.0%, the yield loads of the longitudinal tensile steel bar increased by 8.9%, 3.2%, and 6.6%, and the ultimate loads increased by 9.8%, 2.8%, and 4.2%, respectively. When the I14 steel was replaced with I16 steel, the steel content increased, and the bearing capacity of the specimen, along with the residual bearing capacity remaining after the ultimate bearing capacity had been exceeded, all increased. Increasing the thickness of the section steel web increased the amount of steel used, but the increases in cracking load and bearing capacity were not obvious, and the phenomenon of the sudden drop in bearing capacity due to brittle failure could be fixed. Compared with increasing the thickness of the web, increasing the thickness of the bottom plate increased the cracking load and ultimate load to a greater extent, but the residual load carrying capacity did not change much after the peak load had been exceeded. Increasing the steel content in different ways increased the bearing capacity and stiffness of the specimen, but the ranges of increase differed.
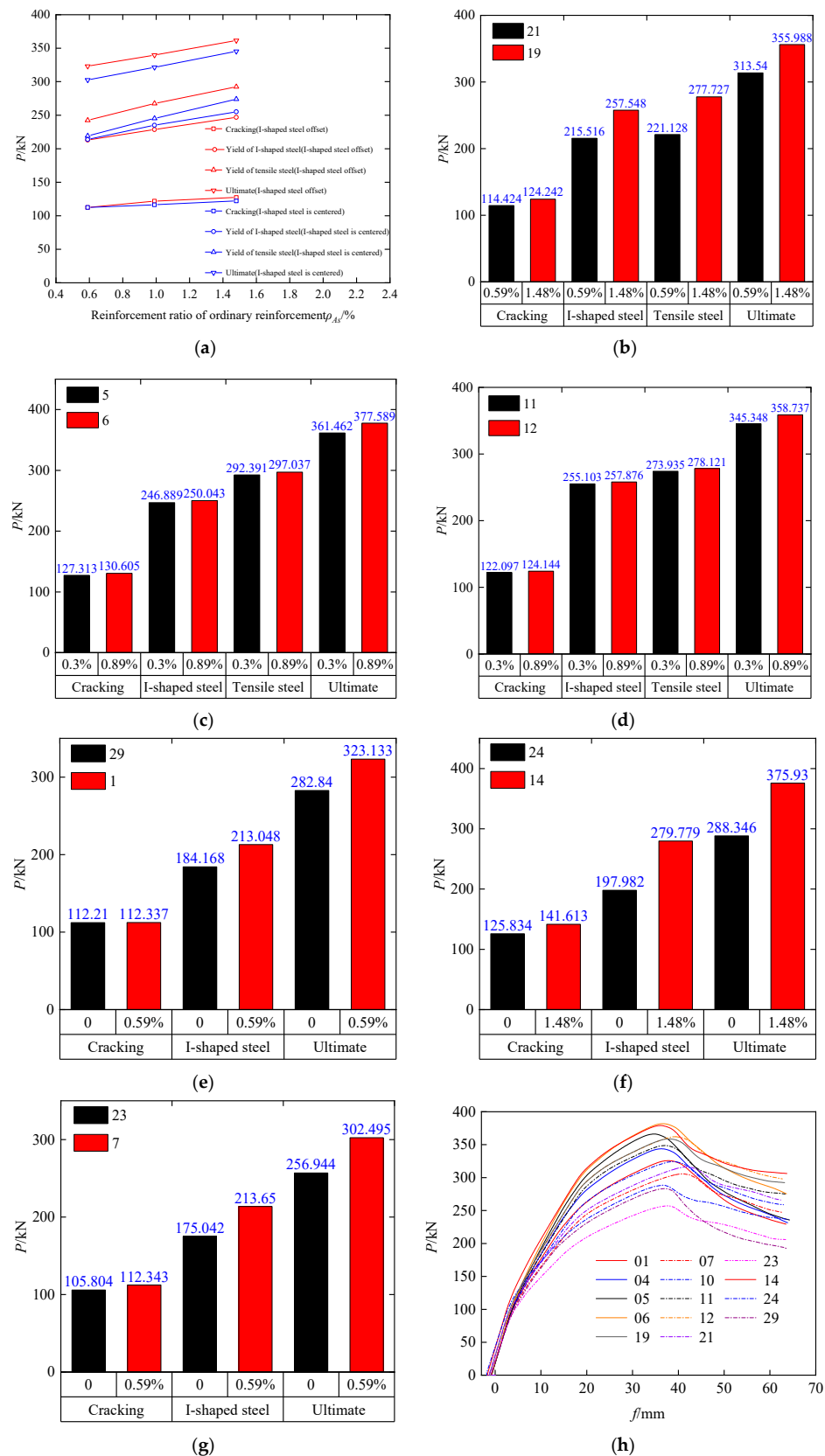
Figure 22. Influence of reinforcement ratio of non-prestressed reinforcement on bearing capacity. (**a**) Reinforcement ratio load curve; (**b**) compare with 19 and 21; (**c**) compare with 5 and 6; (**d**) compare with 11 and 12; (**e**) compare with 1 and 29; (**f**) compare with 14 and 24; (**g**) compare with 7 and 23; (**h**) load–deflection curve.

(**a**)

(**b**)

(**c**)
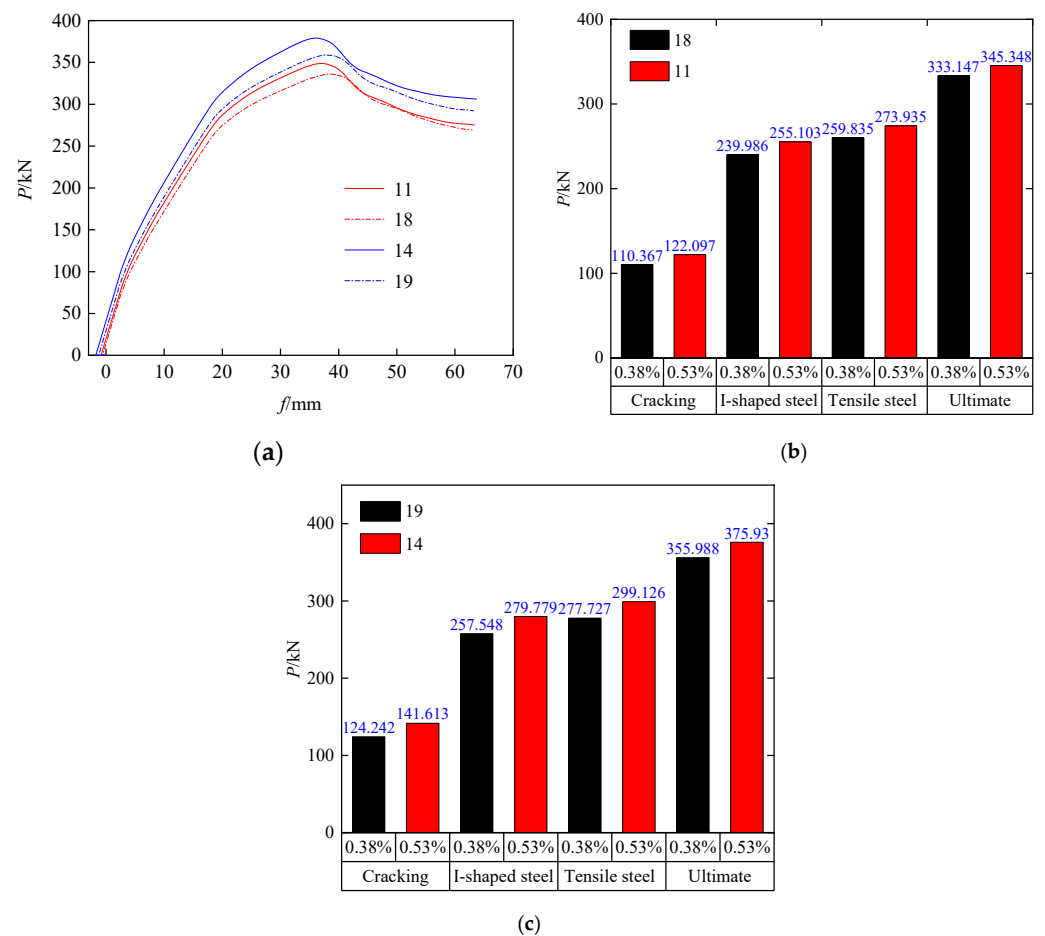
Figure 23. Influence of prestressed reinforcement ratio on bearing capacity. (**a**) Load–deflection curve; (**b**) compare with 1 and 18; (**c**) compare with 14 and 19.

(**a**)

(**b**)
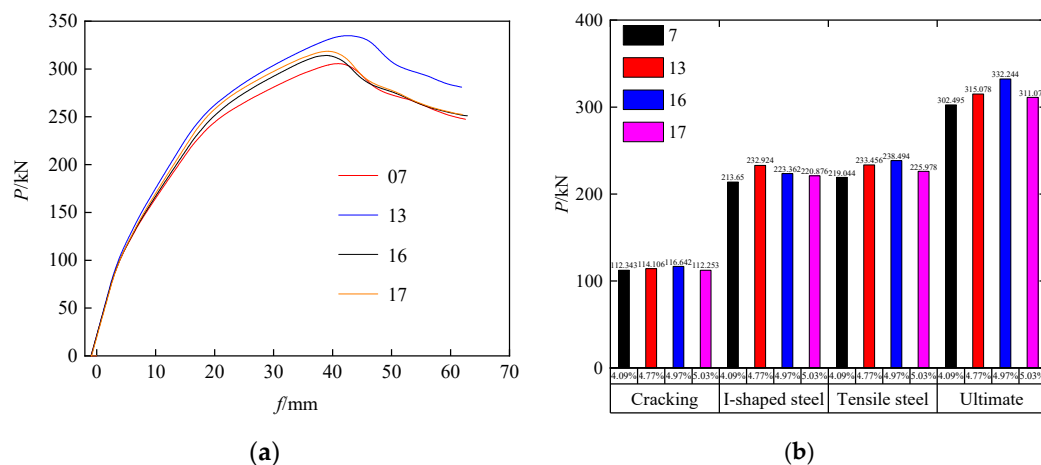
Figure 24. Influence of the ratio of shaped steel bars on the bearing capacity. (**a**) Load–deflection curve; (**b**) compare with 7, 13, 16 and 17.

(4)　Effective prestress

As shown in Figure 25, the values of the tension control stress of the prestressed tendons of PSRUHPC-02, 01, and 03, PSRUHPC-08, 07, and 09, and PSRUHPC-20, 21, and 22 increased from 0.6 f_{ptk} to 0.8 f_{ptk}. Compared with the 02 specimen, the cracking loads of specimens 01 and 03 increased by 2.7% and 15.5%, respectively; the yield loads of the

section steel increased by 5.1% and 11.1%, the yield loads of tensile steel bars increased by 4.3% and 8.4%, and the ultimate loads increased by 2.0% and 3.9%, respectively. Compared with 08, the cracking loads of 07 and 09 increased by 8.2% and 16.4%, the yield loads of section steel increased by 4.9% and 10.1%, the yield loads of the tensile steel bar increased by 4.8% and 9.4%, respectively, and the ultimate load increased by 2.5% and 4.8%, respectively. Compared with 20, the cracking loads of 21 and 22 were increased by 8.4% and 16.6%, the yield loads of the section steel increased by 5.0% and 10.1%, the yield loads of the tensile steel bars increased by 4.7% and 9.1%, and the ultimate loads increased by 2.6% and 5.2% respectively. Increasing the tension control stress of the prestressed tendons significantly increased the cracking load, and the effects on the yield load and stiffness after yielding were basically linear, but with little effect on the ultimate load.

(a)

(b)
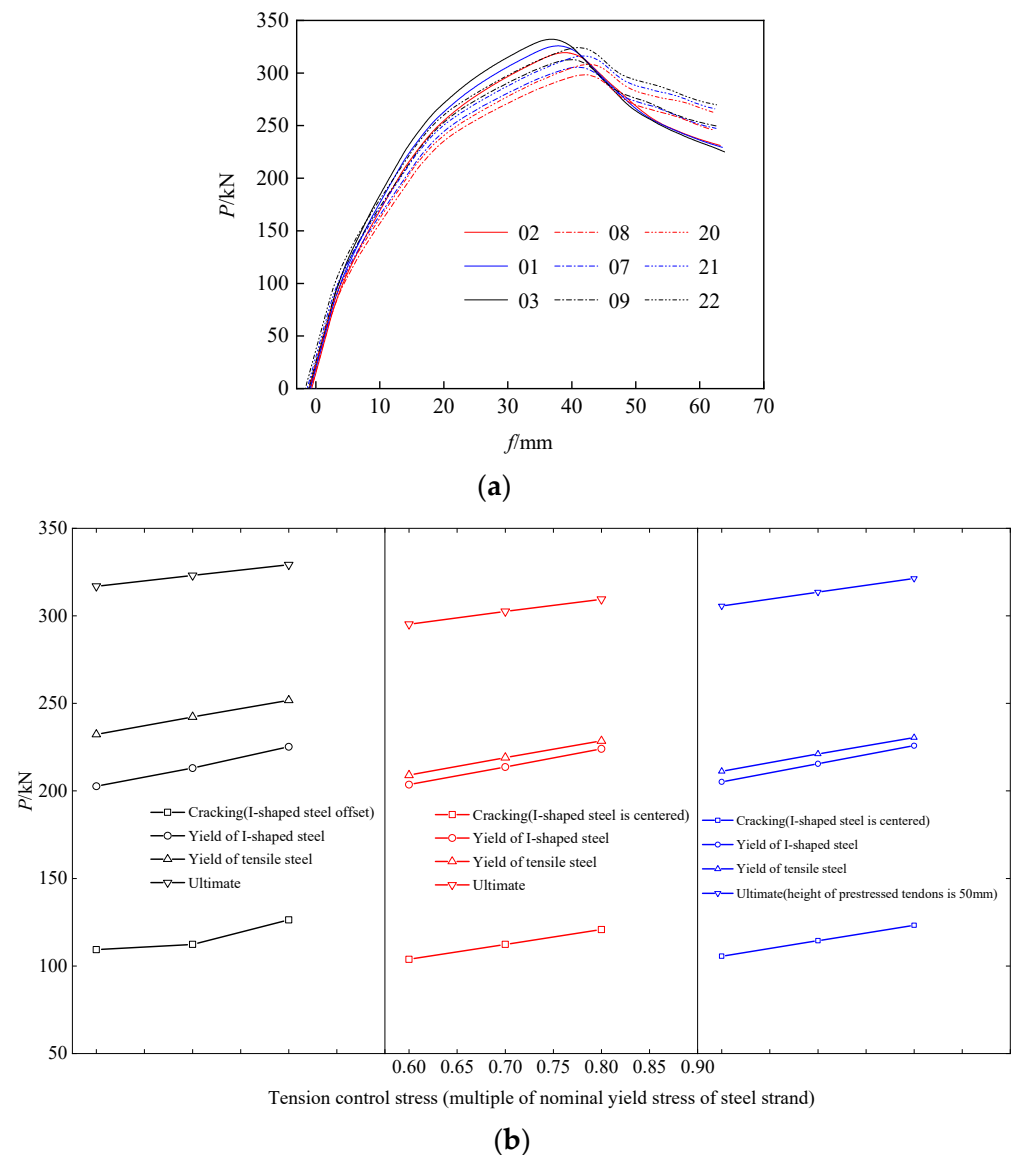
Figure 25. Effect of effective prestress on bearing capacity. (**a**) Load–deflection curve; (**b**) load and effective prestress curve.

(5)   Height of prestressed tendons

As shown in Figure 26, the prestress heights of PSRUHPC-11, 18 and 14, and 19 and 15 were 100 mm, 50 mm, and 70 mm, respectively. Compared with the specimens of 11, the cracking loads of 15 and 14 were increased by 15.9% and 16.0%, respectively, the

yield loads of the I-shaped steel increased by 9.0% and 9.7%, the yield loads of the tensile steel bars increased by 6.1% and 9.2%, and the ultimate loads increased by 4.0% and 8.9%, respectively. With the decrease in the height of the prestressed tendons, the degree of cracking of the specimen was obviously improved, and the increases in yield and ultimate load were basically linear, because the decrease in the height of the prestressed tendons increased the distance metric.
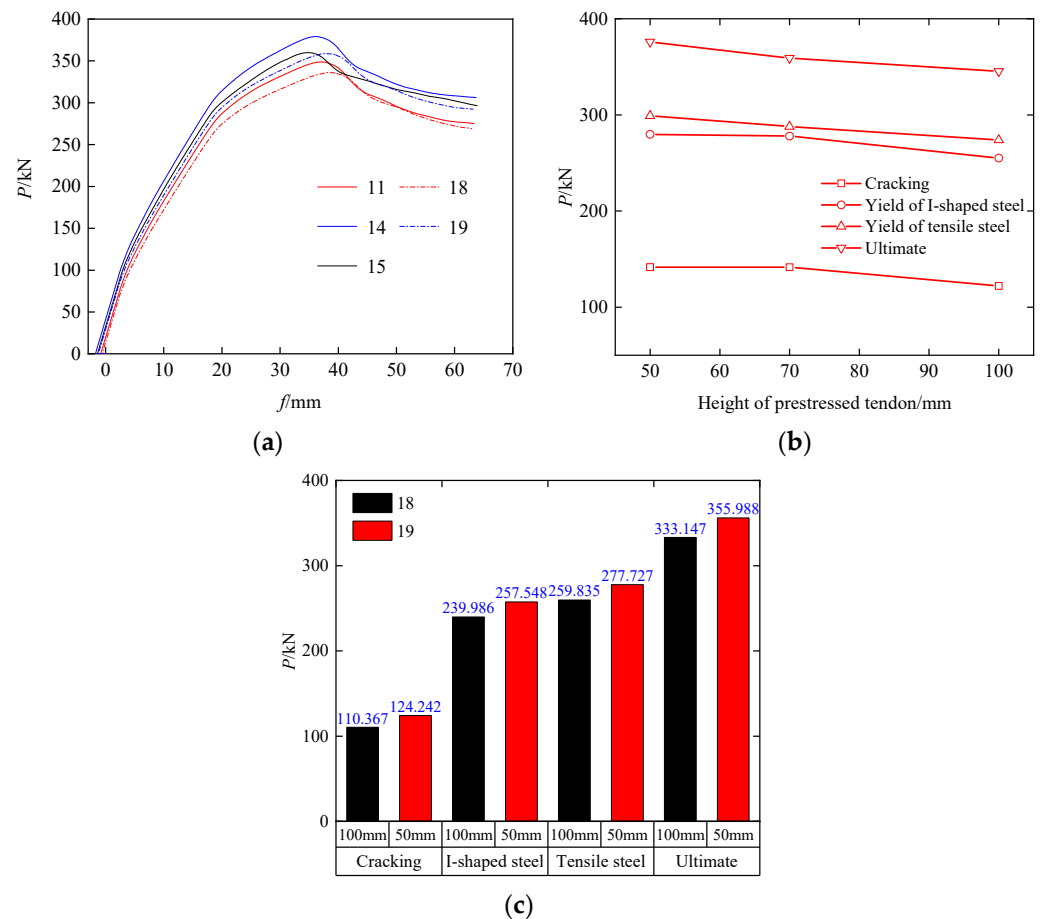
Figure 26. Influence of prestressed tendon height on bearing capacity. (**a**) Load–deflection curve; (**b**) load and height of prestressed tendons curve; (**c**) compare with 18 and 19.

(6) I-shaped steel position

As shown in Figure 27, after the section steel had been arranged in the tension zone, the cracking of the specimen and the yield load of the section steel did not change much, while the yield load of the longitudinal reinforcement and the limit value load increased significantly. Compared with 07, the cracking load and I-shaped steel yield load of 01 were basically unchanged, the tensile steel yield load increased by 10.6%, and the ultimate load increased by 6.8%. Compared with 08, 02 showed a 5.3% increase in cracking load, a 0.5% decrease in I-shaped steel yield load, an 11.1% increase in tensile steel yield load, and a 7.3% increase in ultimate load. Compared with 09, 03 showed a 4.6% increase in cracking load, a 0.5% increase in I-shaped steel yield load, a 10.2% increase in tensile steel yield load, and a 6.4% increase in ultimate load. Compared with 10, the cracking load of 04 was increased by 4.6%, the yield load of the I-shaped steel was reduced by 2.8%, the yield load of the tensile steel bar was increased by 9.1%, and the ultimate load was increased by 5.7%. The cracking load of the specimen did not change much, and the yield load and peak load increased linearly, but the section steel's offset weakened the increase in the reinforcement ratio of non-prestressed tensile bars, thus improving the bearing capacity of the specimen.
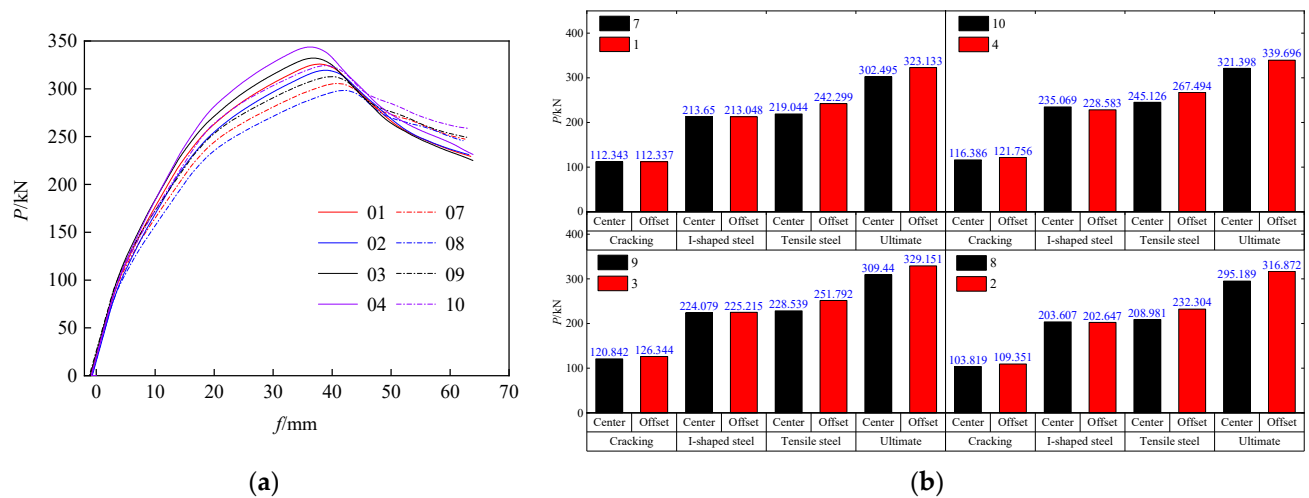
Figure 27. Influence of shaped steel's position on bearing capacity. (**a**) Load–deflection curve; (**b**) comparison diagram.

(7) I-shaped steel strength

As shown in Figure 28, PSRUHPC-25 and 26 corresponded to 01, and 27 and 28 corresponded to 07, in their uses of Q345 and Q420 steel, respectively. After the inclusion of high-strength steel, the tensile longitudinal bars in the center or near-center of the steel being profiled yielded under tension before the bottom plate did, which increased the yield load and ultimate load, but had little effect on increasing the cracking load. It is not recommended that high-strength steel be used to increase bearing capacity.
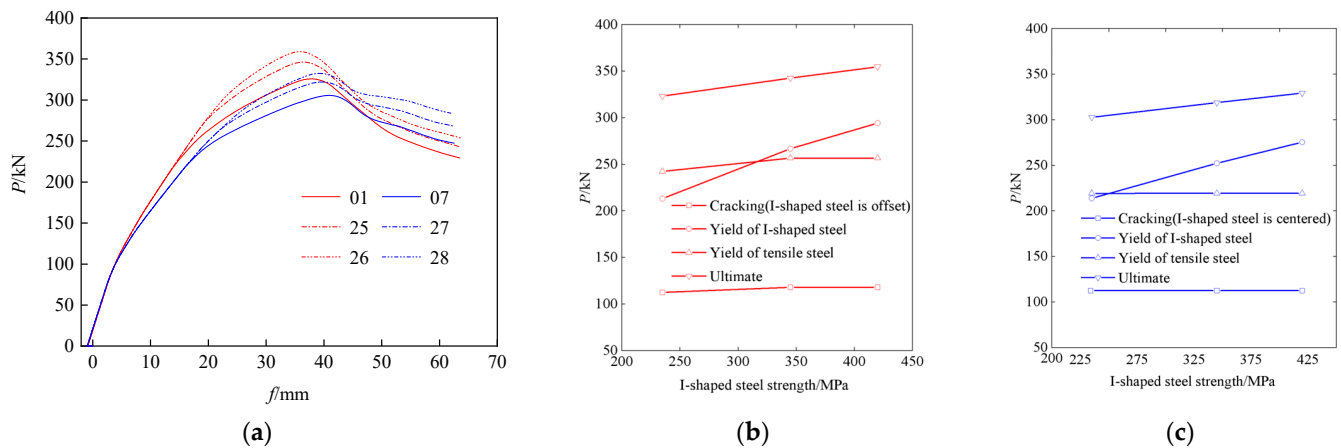
Figure 28. Influence of shaped steel's strength on bearing capacity. (**a**) Load–deflection curve; (**b**) Load-strength curve of section steel at the center; (**c**) Load-strength curve of section steel at the lower.

(8) With or without bonding

As shown in Figure 29, bonded prestressed steel bars were adopted for use in PSRUHPC-30. Compared with 01, the cracking load of this specimen was increased by 2.0%, the yield load of the section steel was increased by 2.2%, the yield load of the tensile steel bars was increased by 2.4%, and the ultimate load was increased by 2.0%. It can be seen that the stiffness of the beam subjected to the simulated bonding method was slightly greater than that of the non-bonded beam, and the cracking load and ultimate load were not greatly improved. The use of unbonded steel strands reduced the amount of construction required, without any loss in the bearing capacity or performance. UHPC can also more effectively prevent the corrosion of unbonded prestressed steel strands.
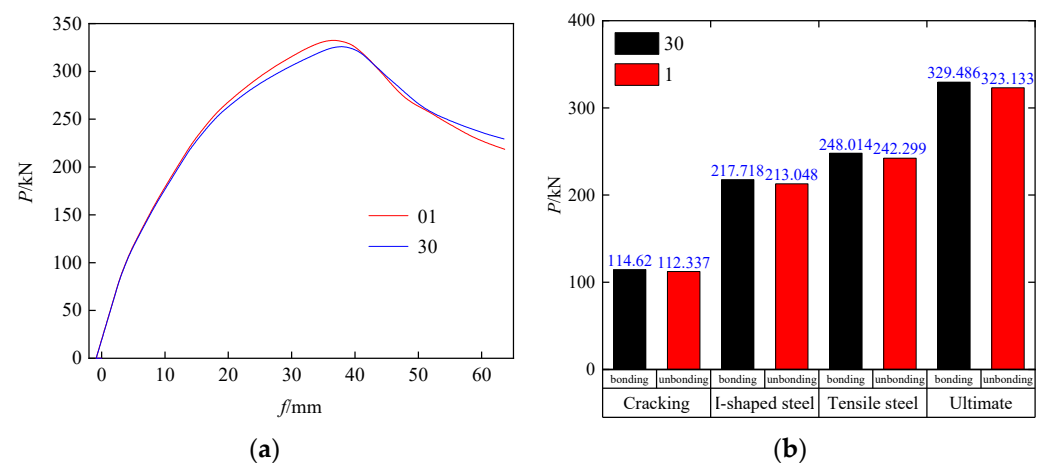
Figure 29. Influence of the presence or absence of bonding on the bearing capacity. (**a**) Load–deflection curve; (**b**) compare with 1 and 30.

4.4.2. Influence of Resistance to Ductility

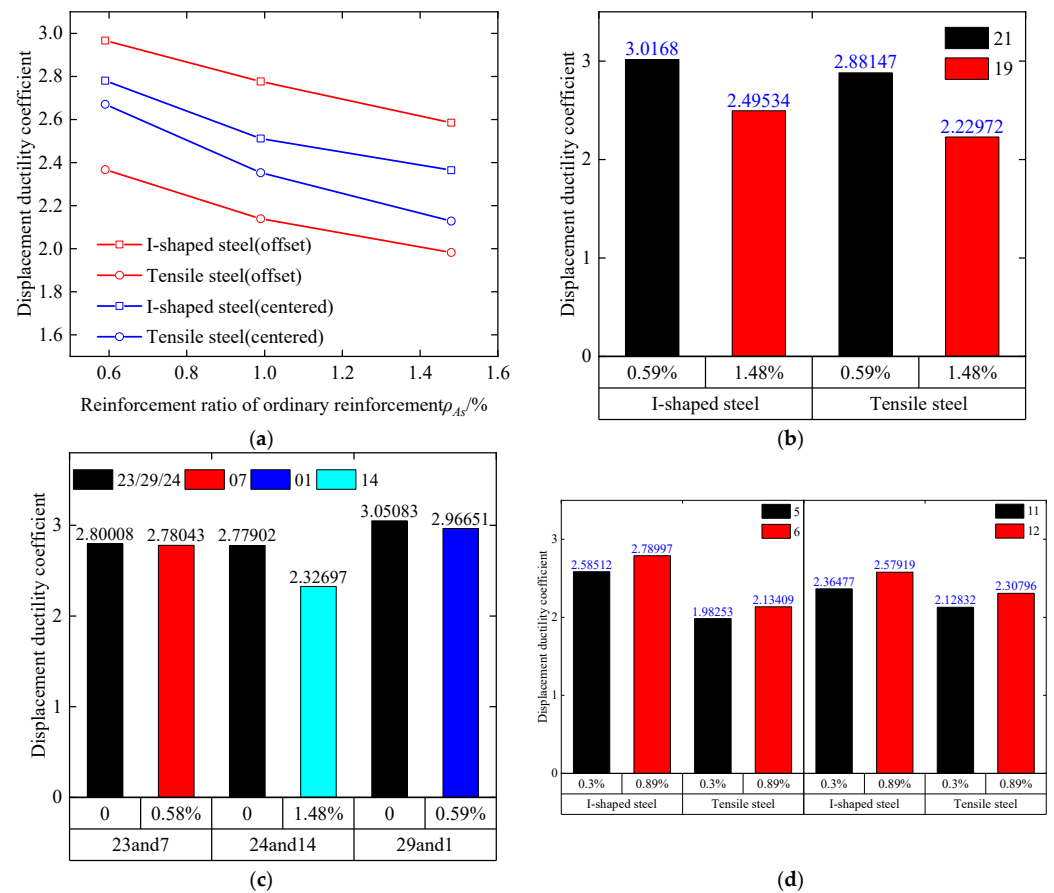(1)   Reinforcement ratio of ordinary reinforcement

As shown in Figure 30a–c, the displacement ductility coefficient decreased with the increase in the reinforcement ratio of the longitudinal non-prestressed tensile steel bars, and the displacement ductility coefficient of the beam increased with the reinforcement ratio of the non-prestressed tensile steel bars. The reason for this is that the reinforcement ratio and the bending stiffness of the specimen both increased, resulting in an increase in the height of the UHPC compression zone and reductions in the final beam displacement and bending ductility values. According to Figure 30d, the bending ductility of the specimen was improved by increasing the reinforcement ratio of the compression steel bar to a certain extent.

(2)   Reinforcement ratio of prestressed tendons

As shown in Figure 31, the flexural ductility of the specimen imparted by the reinforcement ratio of the prestressed reinforcement was similar to that imparted by the non-prestressed tensile reinforcement. With the increase in the reinforcement ratio of the prestressed reinforcement, the displacement ductility coefficient of the specimen decreased. This reduction was more pronounced with the application of prestressed tendons with lower heights.

(3)   Steel content of section steel

As shown in Figure 32, comparing specimens 13, 27 and 07, the steel contents were increased when using larger steel in, and increasing the thickness of, the bottom plate. The increase in the steel content caused the beam displacement ductility coefficient to decrease. The effect of increasing the content of steel was similar to that of increasing its distribution. However, when compared with 07 and 17, the thickness of the web plate increased, the steel content increased, and the displacement ductility coefficient increased, further showing that applying this approach can improve the bearing capacity of the beam in the later stage of loading, and thus prevent the sudden drop in bearing capacity caused by the brittle failure phenomenon in ultra-high-strength UHPC.

Figure 30. Influence of the reinforcement ratio of non-prestressed reinforcement on ductility. (**a**) Ductility and reinforcement ratio curve; (**b**) compare with 19 and 21; (**c**) influence of tensile reinforcement; (**d**) influence of compressive reinforcement.
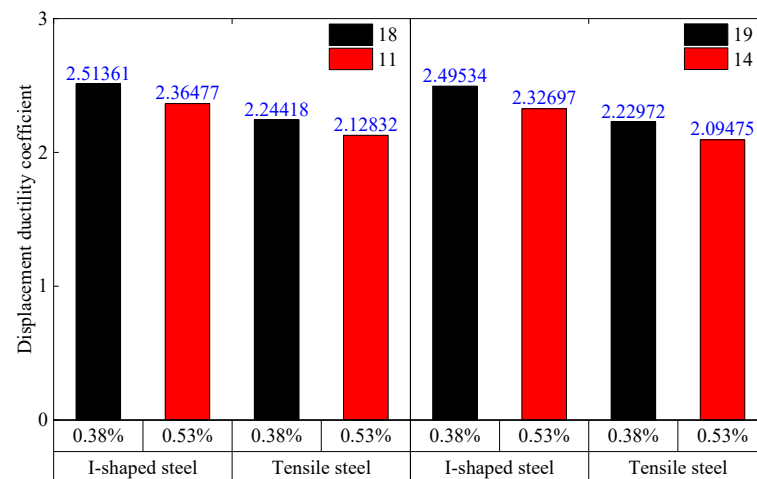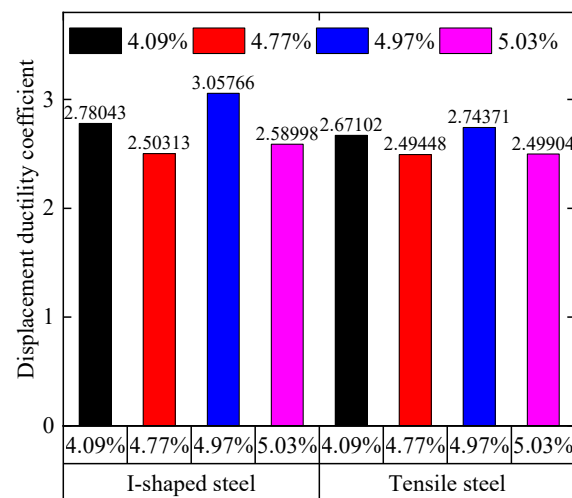

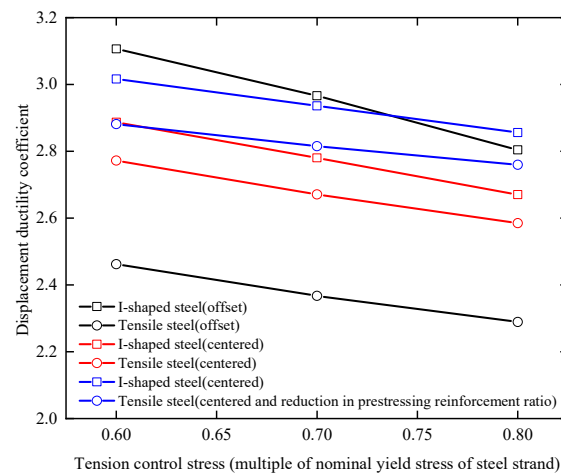**Figure 31.** Influence of prestressing reinforcement ratio on ductility.

(4) Effective prestress

As shown in Figure 33, the displacement ductility coefficient decreased with the increase in the tensile control stress (effective prestress), and the effective prestress had a greater impact on the local ductility coefficient of the profiled beam with offset steel.

Figure 32. Influence of shaped steel ratio on displacement ductility coefficient.

Figure 33. Effect of prestress on ductility.

(5)   Height of prestressed tendons

As shown in Figure 34, the displacement ductility coefficient increased with the increase in the prestressed tendons' height.
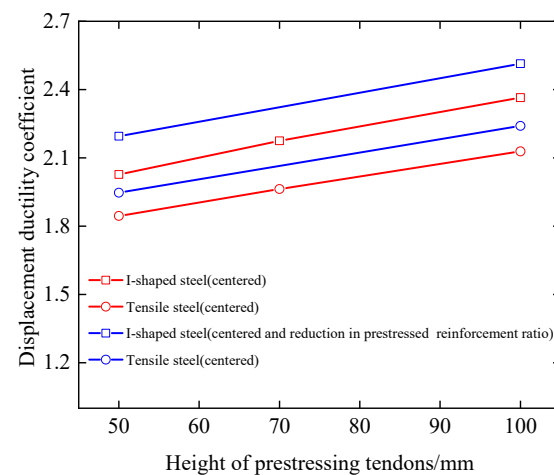
Figure 34. Influence of prestressed tendon height on ductility.

(6)   I-shaped steel position

As shown in Figure 35, after the I-shaped steel had been offset, the displacement ductility coefficient increased from the point of view of the yield of the I-shaped steel, while the displacement ductility coefficient decreased from the point of view of the yield of the tension steel bar. Regardless of whether the I-shaped steel was offset or not, the displacement ductility coefficient decreased nonlinearly with the increase in the non-prestressed tensile steel's reinforcement ratio.

(7)   I-shaped steel strength

It can be seen from Figure 36 that with the increase in the strength of the profiled steel, its bottom plate lags behind its tensile steel bar in terms of yield time, and the beam's displacement ductility coefficient presents a nonlinear, decreasing trend.

(8)   With or without bonding

As shown in Figure 37, when the prestressed steel strand had been bonded, the beam displacement ductility coefficient decreased, but this effect was not obvious. The rigidity of beams could thus be improved by the bonding method, such that their limit displacement can be reduced.
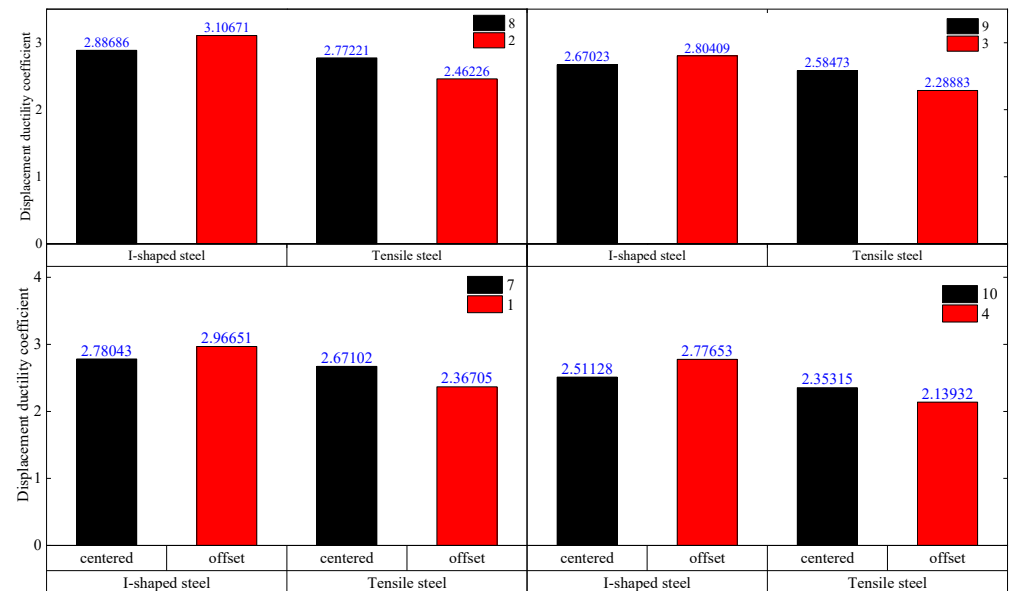

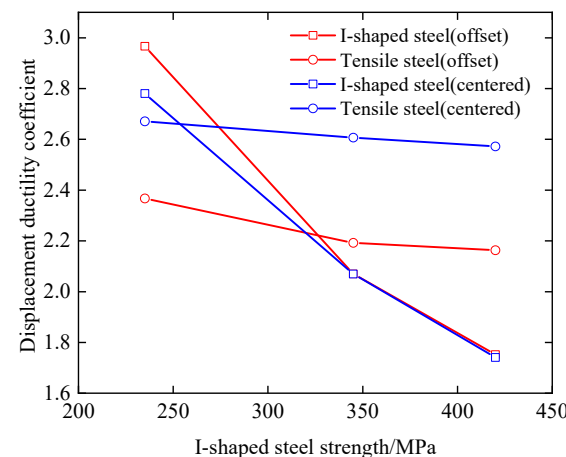**Figure 35.** Influence of shaped steel's position on ductility.

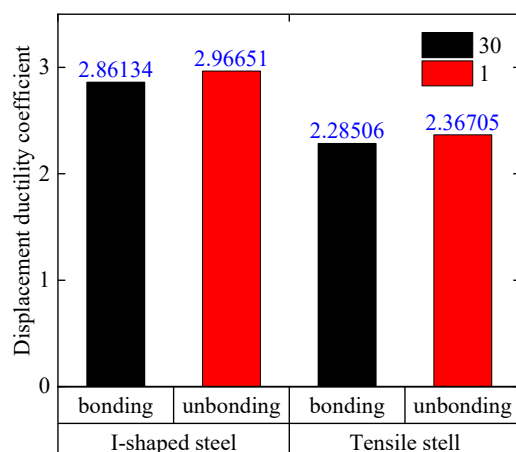**Figure 36.** Influence of shaped steel's strength on ductility.

Figure 37. Influence of the presence or absence of bonding on ductility.

5. Conclusions

1. The test results show that the bending processes of unbonded prestressed steel UHPC (PSRUHPC) beams are similar to those used for ordinary reinforced concrete beams, and UHPC crushing in the compression zone is a sign of failure. Due to the tie effect of steel fibers, the crushed concrete still maintained good integrity, and there was no fragmentation phenomenon; after cracking, the concrete in the tension zone remained functional, and the cracking inflection point of the load–deflection curve was not obvious. The presence of I-shaped steel endowed the PSRUHPC beam with good deformation performance. The application of prestress significantly improved the stiffness of the beam before cracking. The cracking loads of the three test beams accounted for each of their ultimate loads, which were higher than those seen in ordinary concrete beams, and they displayed higher bearing capacities before cracking. At the same height, the change trends of the strain in the section steel and UHPC were roughly the same. After most of the section steel had yielded under tension, the strains of the two deviated, but they were shown to generally work together.

2. The PSRUHPC beam showed a significantly improved bearing capacity, and its bending ductility performance was improved. Compared with PRUHPC beams, PSRUHPC beams showed a bearing capacity increase of 55.3%, a cracking load increase of 11.9%, and a displacement ductility coefficient increase of 76.2%. Compared with SRUHPC beams, PSRUHPC beams showed a 15.4% increase in bearing capacity, a 50.2% increase in cracking load, and a 12.1% increase in displacement ductility coefficient.

3. Due to the diversity in the distribution and orientation of steel fibers in the matrix at the time of pouring, together with the bridging effects of steel fibers, multiple cracking phenomena emerged when the three test beams were flexed and cracked. The cracks did not start from the bottom of the beam, and the initial cracking directions varied and were not perpendicular with the bottom edge of the beam. Using I-shaped steel resulted in finer UHPC cracks.

4. The magnetic flux sensor cable force monitoring system was shown to more effectively monitor the strand stress increment of the unbonded prestressed steel UHPC beam; the load–strand stress increment curves were basically the same as the load–deflection curves, and the stress increment of the steel strand was positively correlated with the midspan deflection.

5. The simulation results show that the reinforcement ratio and the shaped steel content ratio of an ordinary longitudinal reinforcement had a greater impact on the yield load and ultimate load, and the reinforcement ratio of the prestressed reinforcement had a greater impact on the cracking load. Increasing the effective prestress significantly decreased the bending ductility of the beam. As the section steel and the prestressed tendons in the section moved downwards, the beam's bearing capacity increased, but its bending ductility decreased. After incorporating high-strength steel, the yield load

and ultimate load were significantly increased, but the flexural ductility properties of the beam showed a nonlinear, decreasing trend.

References

1. de Larrard, F.; Sedran, T. Optimization of ultra-high-performance concrete by the use of a packing model. *Cem. Concr. Res.* **1994**, *24*, 997–1009. [CrossRef]
2. Yoo, D.-Y.; Banthia, N. Mechanical properties of ultra-high-performance fiber-reinforced concrete: A review. *Cem. Concr. Compos.* **2016**, *73*, 267–280. [CrossRef]
3. Xue, J.; Briseghella, B.; Huang, F.; Nuti, C.; Tabatabai, H.; Chen, B. Review of ultra-high performance concrete and its application in bridge engineering. *Constr. Build. Mater.* **2020**, *260*, 119844. [CrossRef]
4. Zhu, Y.; Zhang, Y.; Hussein, H.H.; Chen, G. Flexural strengthening of reinforced concrete beams or slabs using ultra-high performance concrete (UHPC): A state of the art review. *Eng. Struct.* **2020**, *205*, 110035. [CrossRef]
5. Li, J.; Wu, Z.; Shi, C.; Yuan, Q.; Zhang, Z. Durability of ultra-high performance concrete—A review. *Constr. Build. Mater.* **2020**, *255*, 119296. [CrossRef]
6. Wang, X.; Wu, D.; Zhang, J.; Yu, R.; Hou, D.; Shui, Z. Design of sustainable ultra-high performance concrete: A review. *Constr. Build. Mater.* **2021**, *307*, 124643. [CrossRef]
7. Zhang, Y.; Xin, H.; Correia, J.A. Fracture evaluation of ultra-high-performance fiber reinforced concrete (UHPFRC). *Eng. Fail. Anal.* **2021**, *120*, 105076. [CrossRef]
8. Hu, R.; Fang, Z.; Shi, C.; Benmokrane, B.; Su, J. A review on seismic behavior of ultra-high performance concrete members. *Adv. Struct. Eng.* **2020**, *24*, 1054–1069. [CrossRef]
9. Elmorsy, M.; Hassan, W. Seismic behavior of ultra-high performance concrete elements: State-of-the-art review and test database and trends. *J. Build. Eng.* **2021**, *40*, 102572. [CrossRef]
10. Liu, J.; Li, J.; Fang, J.; Su, Y.; Wu, C. Ultra-high performance concrete targets against high velocity projectile impact—A-state-of-the-art review. *Int. J. Impact Eng.* **2022**, *160*, 104080. [CrossRef]
11. Nabodyuti, D.; Prakash, N. State-of-the-art review on ultra high performance concrete—Ballistic and blast perspective. *Cem. Concr. Compos.* **2022**, *127*, 104383.
12. Bae, B.-I.; Choi, H.-K.; Choi, C.-S. Flexural Strength Evaluation of Reinforced Concrete Members with Ultra High Performance Concrete. *Adv. Mater. Sci. Eng.* **2016**, *2016*, 2815247. [CrossRef]
13. Singh, M.; Sheikh, A.; Ali, M.M.; Visintin, P.; Griffith, M. Experimental and numerical study of the flexural behaviour of ultra-high performance fibre reinforced concrete beams. *Constr. Build. Mater.* **2017**, *138*, 12–25. [CrossRef]
14. Chen, S.; Zhang, R.; Jia, L.-J.; Wang, J.-Y.; Hu, A.; Liang, X.; Yu, J.; Shi, Q.; Yang, I.-H.; Joh, C.; et al. Flexural behaviour of rebar-reinforced ultra-high-performance concrete beams. *Mag. Concr. Res.* **2018**, *70*, 997–1015. [CrossRef]
15. Liu, C.; Zhang, Y.; Yao, Y.; Huang, Y. Calculation Method for Flexural Capacity of High Strain-hardening Ultra-high Performance Concrete T-beams. *Struct. Concr.* **2019**, *20*, 405–419. [CrossRef]
16. Qiu, M.; Shao, X.; Wille, K.; Yan, B.; Wu, J. Experimental Investigation on Flexural Behavior of Reinforced Ultra High Performance Concrete Low-Profile T-Beams. *Int. J. Concr. Struct. Mater.* **2020**, *14*, 5. [CrossRef]
17. Yoo, D.; Yoon, Y. A Review on Structural Behavior, Design, and Application of Ultra-High-Performance Fiber- Reinforced Concrete. *Struct. Des.* **2016**, *10*, 125–142. [CrossRef]
18. Chen, B.; Ji, T.; Huang, Q.; Wu, H.; Ding, Q.; Zhan, Y. Review of Ultra High Performance Concrete Research. *Chin. J. Build. Sci. Eng.* **2014**, *31*, 1–24.
19. Hung, C.-C.; El-Tawil, S.; Chao, S.-H. A Review of Developments and Challenges for UHPC in Structural Engineering: Behavior, Analysis, and Design. *J. Struct. Eng.* **2021**, *147*, 03121001. [CrossRef]
20. Zhang, P.; Lv, X.; Liu, Y.; Zou, X.; Li, Y.; Wang, J.; Sheikh, S.A. Novel fiber reinforced polymers (FRP)-ultrahigh performance concrete (UHPC) hybrid beams with improved shear performance. *Constr. Build. Mater.* **2021**, *286*, 122720. [CrossRef]
21. El-Hacha, R.; Chen, D. Behaviour of hybrid FRP–UHPC beams subjected to static flexural loading. *Compos. Part B Eng.* **2012**, *43*, 582–593. [CrossRef]

22. Naaman, A.; Alkhairi, F. Stress at ultimate in unbonded post-tensioning tendons. Part 2. Proposed methodology. *ACI Struct. J.* **1991**, *88*, 683–692.
23. Mohamed, H.H. Effect of Span-Depth Ratio on the Ultimate Steel Stress in Unbonded Prestressed concrete members. *ACI Struct. J.* **1990**, *87*, 305–312.
24. Qin, Z.; Deng, N. Simulation Experiment and Application of Magneto-Elastic Sensor for Optimal Magnetization Model. *J. Shijiazhuang Tiedao Univ. (Nat. Sci. Ed.)* **2022**, *35*, 70–75.
25. Wang, X.; Liu, H.; Ju, Y.; Wang, D. Experimental and analytical models of flexural behavior of U-shaped reactive powder concrete permanent beam formworks. *Constr. Build. Mater.* **2021**, *300*, 123670. [CrossRef]
26. Turker, K.; Torun, I.B. Flexural performance of highly reinforced composite beams with ultra-high performance fiber reinforced concrete layer. *Eng. Struct.* **2020**, *219*, 110722. [CrossRef]
27. Tanarslan, H.M.; Alver, N.; Jahangiri, R.; Yalçınkaya, Ç.; Yazıcı, H. Flexural strengthening of RC beams using UHPFRC laminates: Bonding techniques and rebar addition. *Constr. Build. Mater.* **2017**, *155*, 45–55. [CrossRef]
28. Safdar, M.; Matsumoto, T.; Kakuma, K. Flexural behavior of reinforced concrete beams repaired with ultra-high performance fiber reinforced concrete (UHPFRC). *Compos. Struct.* **2016**, *157*, 448–460. [CrossRef]
29. Noshiravani, T.; Brühwiler, E. Analytical Model for Predicting Response and Flexure-Shear Resistance of Composite Beams Combining Reinforced Ultrahigh Performance Fiber-Reinforced Concrete and Reinforced Concrete. *J. Struct. Eng.* **2014**, *140*, 04014012. [CrossRef]
30. Li, S.; Zhang, L.; Guo, P.; Zhang, P.; Wang, C.; Sun, W.; Han, S. Characteristic analysis of acoustic emission monitoring parameters for crack propagation in UHPC-NC composite beam under bending test. *Constr. Build. Mater.* **2021**, *278*, 122401. [CrossRef]
31. Lampropoulos, A.P.; Paschalis, S.A.; Tsioulou, O.T.; Dritsos, S.E. Strengthening of reinforced concrete beams using ultra high performance fibre reinforced concrete (UHPFRC). *Eng. Struct.* **2016**, *106*, 370–384. [CrossRef]
32. Habel, K.; Denarié, E.; Brühwiler, E. Structural Response of Elements Combining Ultrahigh-Performance Fiber-Reinforced Concretes and Reinforced Concrete. *J. Struct. Eng.* **2006**, *132*, 1793–1800. [CrossRef]
33. Dong, Z.; Wu, G.; Zhu, H.; Zhao, X.-L.; Wei, Y.; Qian, H. Flexural behavior of seawater sea-sand coral concrete–UHPC composite beams reinforced with BFRP bars. *Constr. Build. Mater.* **2020**, *265*, 120279. [CrossRef]
34. Al-Osta, M.; Isa, M.; Baluch, M.; Rahman, M. Flexural behavior of reinforced concrete beams strengthened with ultra-high performance fiber reinforced concrete. *Constr. Build. Mater.* **2017**, *134*, 279–296. [CrossRef]
35. Zhu, Y.; Zhang, Y.; Hussein, H.H.; Cai, S. Flexural Study on UHPC–Steel Composite Beams with Joints under Negative Bending Moment. *J. Bridg. Eng.* **2020**, *25*, 04020084. [CrossRef]
36. Wang, Z.; Nie, X.; Fan, J.-S.; Lu, X.-Y.; Ding, R. Experimental and numerical investigation of the interfacial properties of non-steam-cured UHPC-steel composite beams. *Constr. Build. Mater.* **2019**, *195*, 323–339. [CrossRef]
37. Shao, X.; Yi, D.; Huang, Z.; Zhao, H.; Chen, B.; Liu, M. Basic Performance of the Composite Deck System Composed of Orthotropic Steel Deck and Ultrathin RPC Layer. *J. Bridg. Eng.* **2013**, *18*, 417–428. [CrossRef]
38. Luo, J.; Shao, X.; Cao, J.; Xiong, M.; Fan, W. Transverse bending behavior of the steel-UHPC lightweight composite deck: Orthogonal test and analysis. *J. Constr. Steel Res.* **2019**, *162*, 105708. [CrossRef]
39. Liu, X.; Zhang, J.; Cheng, Z.; Ye, M. Experimental and Numerical Studies on the Negative Flexural Behavior of Steel-UHPC Composite Beams. *Adv. Civ. Eng.* **2021**, *2021*, 8828175. [CrossRef]
40. Choi, W.; Choi, Y.; Yoo, S.-W. Flexural Design and Analysis of Composite Beams with Inverted-T Steel Girder with Ultrahigh Performance Concrete Slab. *Adv. Civ. Eng.* **2018**, *2018*, 1356027. [CrossRef]
41. Tu, N.; Raad, M. Flexural Performance of Composite Ultra-High-Performance Concrete-Encased Steel Hollow Beams. *Civ. Eng. J.* **2019**, *5*, 1289–1304.
42. Tu'ma, N.H.; Hammood, M.N.; Mohsin, R.D. Flexural Strength Estimation for Hollow Cross-Section Simply Supported UHPC Beams. *Civ. Environ. Eng.* **2018**, *17*, 476–484. [CrossRef]
43. Liangtao, B.; Ding, L. Experimental study on flexural properties of steel beams with reactive powder concrete outsourcing. *Chin. J. Railw. Sci. Eng.* **2018**, *15*, 389–397.
44. Bu, L.; Teng, D. Experimental of mechanical performance of shaped steel encircled with reactive powder concrete composite beams. *J. Wuhan Univ. (Eng. Ed.)* **2018**, *51*, 721–726+731.
45. Bu, L.; Luo, K. Internface Bonding Performance Between Shape Steel and Reactive Powder Concrete (RPC) in Steel Reinforced RPC structures. *Sci. Technol. Eng.* **2018**, *18*, 307–312.
46. Bu, L.; Tang, C. Experimental Study on Flexural Behavior of I-section Steel Ultra High Performance Concrete (UHPC) Beams. *Highw. Eng.* **2021**, *46*, 1–7+65.
47. Huang, Z.; Huang, X.; Li, W. Bond-slip behaviour of H-shaped steel embedded in UHPFRC. *Steel Compos. Struct.* **2021**, *38*, 563–582.
48. Wang, X. Study on Bond Slip Behavior of Section Steel and Reactive Powder Concrete at Room Temperature. Master's Thesis, Shandong Jianzhu University, Shandong, China, 2020.
49. Zhong, Z. Experimental Study on Bond Slip Behavior of Shaped Steel Reactive Powder Concrete. Master's Thesis, Yangzhou University, Yangzhou, China, 2021.
50. Shao, X.; Ying-Li, R.; Zhao, X. Experimental Study on Flexural Behavior of Joint in Negative Moment Area at Pier Top of Hot Rolled-shape steel-UHPC Composite Continuous Beam. *Chin. J. Highw. Eng.* **2023**, *36*, 34–47.

51. Ye, J. Study on Calculation Method of Rigidity and Crack Width for Steel Section RPC Simply Supported Beam. Master's Thesis, Yangzhou University, Yangzhou, China, 2021.
52. Federation, C.B.M. *Basic Properties and Test Methods of Ultra-High Performance Concrete*; Construction Industry Press: Beijing, China, 2018.
53. Committe, N.C.S.T. *Reactive Powder Concrete*; Construction Industry Press: Beijing, China, 2015.
54. Deng, N.; Long, Y.; Sun, L.; Xia, D. Magnetic flux sensor and its application in bridge engineering. In Proceedings of the 18th National Bridge Academic Conference, Tianjing, China, 1–2 May 2008; pp. 643–648.
55. Jia, J.; Meng, G.; Zhu, W. Experimental study on flexural performance and bearing capacity analysis of prestressed steel ultra-high-strength concrete composite beams. *J. Build. Struct.* **2014**, *35*, 1–10.
56. Li, F. Experimental Research on Bearing Capacity of Prestressed Steel Reinforced Concrete Beams. Master's Thesis, Chongqing University, Chongqing, China, 2007.
57. Fu, C.; Li, Y.; Liang, S. Experimental study on flexural performance of prestressed steel-concrete simply supported beams. *J. Build. Struct.* **2007**, *3*, 62–73.
58. Tang, C.; Zhou, K.; Zhang, B. Experimental study on flexural bearing capacity of unbonded prestressed steel-concrete beams. *J. Railw. Sci. Eng.* **2018**, *15*, 1271–1277.
59. Su, J.-Z.; Ma, X.-L.; Chen, B.-C.; Sennah, K. Full-scale bending test and parametric study on a 30-m span prestressed ultra-high performance concrete box girder. *Adv. Struct. Eng.* **2019**, *23*, 1276–1289. [CrossRef]
60. Lv, L.; Wang, Y.; Fu, C.; Zheng, W. Values of basic mechanical properties of reactive powder concrete. *J. Harbin Inst. Technol.* **2014**, *46*, 1–9.
61. Li, H.; Guo, X.; Duan, J. Numerical Simulation of Steel-Reinforced Reactive Powder Concrete Beam Based on Bond-Slip. *Materials* **2021**, *14*, 4176. [CrossRef]
62. Loi, T. Research on Finite Element Modeling and Performance Analysis of Unbonded Prestressed Beams. Master's Thesis, Zhejiang University, Zhejiang, China, 2005.